REPORT DOCUMENTATION PAGE

Form Approved
OMB No. 0704-0188

1. REPORT DATE *(DD-MM-YYYY)*	**2. REPORT TYPE**	**3. DATES COVERED** *(From - To)*
20-06-2019	Final Technical	From 06/01/2016- To 05/30/2019

4. TITLE AND SUBTITLE
The Effect of Spatial Heterogeneities on the Transformation Kinetics in Amorphous Al Alloys

5a. CONTRACT NUMBER

5b. GRANT NUMBER
N00014-16-1-2401

5c. PROGRAM ELEMENT NUMBER

6. AUTHOR(S)
Professor John H. Perepezko

5d. PROJECT NUMBER

5e. TASK NUMBER

5f. WORK UNIT NUMBER

7. PERFORMING ORGANIZATION NAME(S) AND ADDRESS(ES)
UNIVERSITY OF WISCONSIN SYSTEMRESEARCH & SPONSORED PROGRAMS21 N PARK ST STE 6401MADISON WI 53715-1218UNITED STATES OF AMERICA

8. PERFORMING ORGANIZATION REPORT NUMBER

9. SPONSORING/MONITORING AGENCY NAME(S) AND ADDRESS(ES)
Office of Naval Research875 N. Randolph Street Suite 1425Arlington VA 22203-1995

10. SPONSOR/MONITOR'S ACRONYM(S)

11. SPONSOR/MONITOR'S REPORT NUMBER(S)

12. DISTRIBUTION/AVAILABILITY STATEMENT
UU
Approved for Public Release

13. SUPPLEMENTARY NOTES

14. ABSTRACT
As part of our continuing study we have discovered that minor (i.e. 1%) solute substitutions to AlYFe amorphous alloys can shift the glass transition temperature, Tg and the crystallization onset, Tx by about 50 K. These changes are correlated with the nucleation delay time. We have developed an innovative method to detect the nucleation delay time. We have identified a double time-temperature – transformation (TTT) curve for the crystallization of a Zn based metallic glass (MG). As an application of controlled spatial heterogeneities we have developed a new class of AlSm-based MGs, which show polymer-like thermoplastic formability near the boiling point (100 °C) of water.

15. SUBJECT TERMS
Amorphous alloys, nucleation, transformation kinetics, spatial heterogeneities

16. SECURITY CLASSIFICATION OF:			**17. LIMITATION OF ABSTRACT**	**18. NUMBER OF PAGES**	**19a. NAME OF RESPONSIBLE PERSON**
a. REPORT	**b. ABSTRACT**	**c. THIS PAGE**			John H. Perepezko
					19b. TELEPHONE NUMBER *(Include area code)*
U	U	U	UU		608-263-1678

Table of Contents

Contract Number: N000141612401
Title: The Effect of Spatial Heterogeneities on the Transformation Kinetics in Amorphous Al Alloys

Summary

The principal goal of the project is a focus on the examination of the influence of spatial heterogeneities on phase transformation behavior. Towards this goal we have identified amorphous Al alloys as an attractive candidate since amorphous alloys are known to exhibit medium range order, MRO which we hypothesized could act as a spatial heterogeneity. For aluminum based metallic glasses, number densities of Al nanocrystals as high as 10^{21} m^{-3} to 10^{23} m^{-3} can develop during the primary crystallization reaction. From a detailed determination of the nucleation kinetics and characterization of the MRO by fluctuation electron microscopy we have developed a new nucleation model based upon MRO catalyzed nucleation of Al nanocrystals that quantitatively accounts for the observed behavior. The details of this part of the project work have been given in previous reports and are not repeated. As part of our continuing study we have discovered that minor (i.e. 1%) solute substitutions to AlYFe amorphous alloys have a large effect on the glass transition temperature, Tg and the crystallization onset, Tx and can shift these temperatures by about 50 K. These changes have been directly correlated with the delay time for the onset of nucleation. These effects are being examined further in terms of the nucleation behavior. With ultra-high heating and cooling rates, Flash DSC can avoid the crystallization during the heating and cooling processes and detect the Tg signal which could be hardly observed by the regular DSC. With the aid of the Flash DSC, we have developed an innovative method to detect the delay time, thus helping us to understand the diffusion behavior of the glass and the origin of the doping effect. We have also completed a new study on the crystallization of a Zn based metallic glass where we have identified a double time-temperature – transformation (TTT) curve for the crystallization to the same product phases. Moreover, the TTT curves for isothermal annealing based upon direct cooling of the liquid and upon upquenching from the amorphous state are different. The different kinetic behavior reveals that the spatial heterogeneities are inherited from the liquid during rapid cooling and the density of spatial heterogeneities is directly related to the rate of cooling. For this novel behavior we have developed an original heterogeneous nucleation analysis that includes the influence of spatial heterogeneities. As a potential application of controlled spatial heterogeneities we have developed a new class of AlSm-based metallic glasses (MGs), which behave with polymer-like thermoplastic formability near the boiling point (100 °C) of water. Overall, the results of the project research enhance our understanding of the role of spatial heterogeneities on transformation behavior and provide new opportunities for research and applications.

Part I

Minor alloying effect on the nucleation dynamics and glass formation ability of $Al_{88}Y_7Fe_5$ metallic glasses via ultrafast Flash DSC

1. Introduction

For Al-based metallic glasses (MGs), the nucleation and crystallization behaviors have gained much attention because of their importance in understanding the fundamental transport process and in the synthesis of nanostructured materials [1-3]. From the microscopic perspective, nucleation can be considered as a process that involves the formation of clusters of atoms as embryos that will develop into nuclei when their size reaches the critical size. Thus, the whole nucleation and crystallization process usually includes transient nucleation, steady state nucleation, crystal growth and coarsening. At one temperature, instead of devitrifying directly, the amorphous samples undergo a period of delay time (or transient time) τ before the obvious precipitation of the crystals [4-5]. The delay time τ characterizes the duration for the establishment of the steady state nucleation rate [6-7]. Thus, the delay time is crucial for understanding of the transport and nucleation behaviors for Al-based MGs. Moreover, the delay time provides the critical information about the glass formation ability. For example, a longer delay time at one temperature endows the higher thermal stability and the better glass formation ability, which is critical for developing bulk Al-based MGs [8]. Meanwhile, there have been many researches focusing on the minor alloying effect in Al-based MGs [9-13]. A clear finding is that the crystallization behavior and glass formation ability are very sensitive to the minor alloying additions [9-13]. However, due to the unknown atomic structure and unavailable experimental tools, the microscopic atomic transport mechanism of the minor alloying effect is still unclear. On the other hand, considering that the delay time is directly related to the atomic diffusion motion [14-17], the delay time can provide a new perspective to investigate the microscopic diffusion mechanism during nucleation. Therefore, more knowledge about the delay time for primary crystallization is necessary for developing the bulk Al-based MGs and understanding the microscopic mechanism of the minor alloying effect.

For the systems such as Zr-, Pd- and Ce-based MGs with good glass formation ability, the crystallization signal is strong enough to show up in the isothermal annealing DSC trace, which makes it possible to directly measure the delay time for crystallization by isothermal tests [18-19]. However, for some marginal MGs, such as Al-based MGs with poor glass formation ability, there usually appears a primary nucleation peak for Al nanocrystals followed by secondary or tertiary crystallization reactions involving intermetallic phases [20-21]. The signal from the primary nucleation of the precipitation of Al_{fcc} nanocrystals is so weak that the crystallization peak is difficult to detect in the isothermal DSC tests [22]. Thus, based on the definition of delay time, the transmission electron microscopy (TEM) method by plotting particle number density and annealing time and then extrapolating the steady state nucleation slope to the time axis was applied to establish the delay time [23]. However, this method is time-consuming and is not a preferential method. For marginal MG systems that exhibit a primary crystallization reaction, there is a composition change in the amorphous matrix. Under isothermal treatment, the evolution of glass transition temperature with annealing time follows different evolution paths before and after crystallization: relaxation effect [24-26] and composition effect [27-29], respectively. From this viewpoint, the break point in the trend of the glass transition temperature change during annealing from the relaxation effect to composition effect should correspond to the delay time for primary

crystallization. Unfortunately, for marginal Al-based MGs, it is difficult to observe an obvious glass transition signal by conventional thermo-analytical methods (DSC and DTA) [18-19]. Recently, a chip-based fast differential scanning calorimeter with orders of magnitude higher heating and cooling was developed and the commercial Flash DSC instrument (Mettler Toledo Flash DSC 1) can reach maximum heating and cooling rates of several 10^4 K/s and 10^3 K/s respectively [30-31]. Based on the Flash DSC, it has been shown to be possible to separate the glass transition and primary crystallization signals at high heating rates [32-33], which provides the foundation for the present study to investigate the delay time for primary crystallization and the effect of minor alloying in Al-based MG systems.

2. Experimental

2.1. Sample preparation

The ingots with compositions of $Al_{88}Y_7Fe_5$, $Al_{87}Y_7Fe_6$, $Al_{87}Y_7Fe_5Cu_1$, $Al_{88}Y_6Fe_5Cu_1$ and $Al_{88}Y_7Fe_4Cu_1$ were produced by arc melting of pure elements for five times to ensure the homogeneity. Amorphous ribbons for the above compositions were formed by single-roller melt spinning on a copper wheel with a tangential speed from 5 m/s to 55 m/s. The thickness of the prepared ribbons was approximately 20 μm and the width of the ribbons was about 2 mm. Both the ingot melting and melt spinning were performed in an inert argon atmosphere to prevent oxidation. The amorphous nature of these ribbons was confirmed by X-ray diffraction (Bruker D8 Discover Diffraction with Cu K_α radiation), and differential scanning calorimetry (PerkinElmer DSC Diamond).

2.2. Thermal and structural analysis

A Diamond DSC instrument was used to measure the thermodynamic and kinetic parameters and perform the isothermal tests. A high-rate Flash DSC instrument with chip sensors (FlashDSC1, Mettler Toledo) was applied to perform the in-situ continuous heating, annealing treatments and the following thermal analyses. The maximum heating and cooling rates for this Flash DSC instrument are 4×10^4 and 4×10^3 K/s and the temperature range is between -90 ^{o}C and 450 ^{o}C. To load the sample onto the chip, the ribbon samples were firstly cut into tiny pieces of 0.15 mm × 0.15 mm and then were loaded into the sample unit of Flash DSC chip by a thin hair. Considering that the Al-based MGs cannot be melted within the Flash DSC temperature limit (450 ^{o}C), separate sample pieces from the same ribbon sample were replaced for every test.

To determine structural information for the Flash DSC samples for different annealing states, a series of TEM tests were performed. The TEM samples from the annealed Flash DSC samples were prepared by Zeiss Auriga Focused Ion Beam (FIB) and a 10 nA FIB current and 2 kV voltage were used to avoid sample damage. After obtaining the TEM samples, the TEM measurements were conducted on a Tecnai T12 instrument at 120 kV.

3. Results and discussion

3.1. Delay time determination for the $Al_{87}Y_7Fe_6$ MG based on the Flash DSC

3.1.1. Glass transition temperature measurement for Al-based MGs

For most MG systems with good glass formation ability, the glass transition signal is strong enough to be detected in the heating DSC traces, which makes it possible to measure the glass transition temperature and the supercooled liquid region by the conventional DSC method. However, for

marginal Al-based MGs, the glass transition signal is prone to be overlapped by a primary crystallization for Al nanocrystals precipitation [9, 11]. Thus, the traditional DSC is not a good thermal analysis tool to observe the glass transition of Al-based MGs. On the other hand, considering that the glass transition and crystallization are significantly different kinetic processes, they should follow different evolution paths with different heating rates, so that the two kinetic signals should be separated under higher heating rates. For example, for a $Al_{87}Y_7Fe_6$ MG, the conventional DSC with heating rate of 20 K/min (0.33 K/s) was applied to measure the heat flow curve shown in Fig. 1(a). It is clear to see that the conventional DSC heat flow curve only displays the primary and secondary crystallization peaks as shown in Fig. 1(b) and there is no clearly defined glass transition signal. In contrast, a typical heat flow curve measured by Flash DSC with the heating rate of 400 K/s is displayed in Fig. 1(b). The optical picture of small sample being loaded onto the Flash DSC chip is shown in the insertion of Fig. 1(b). It is evident

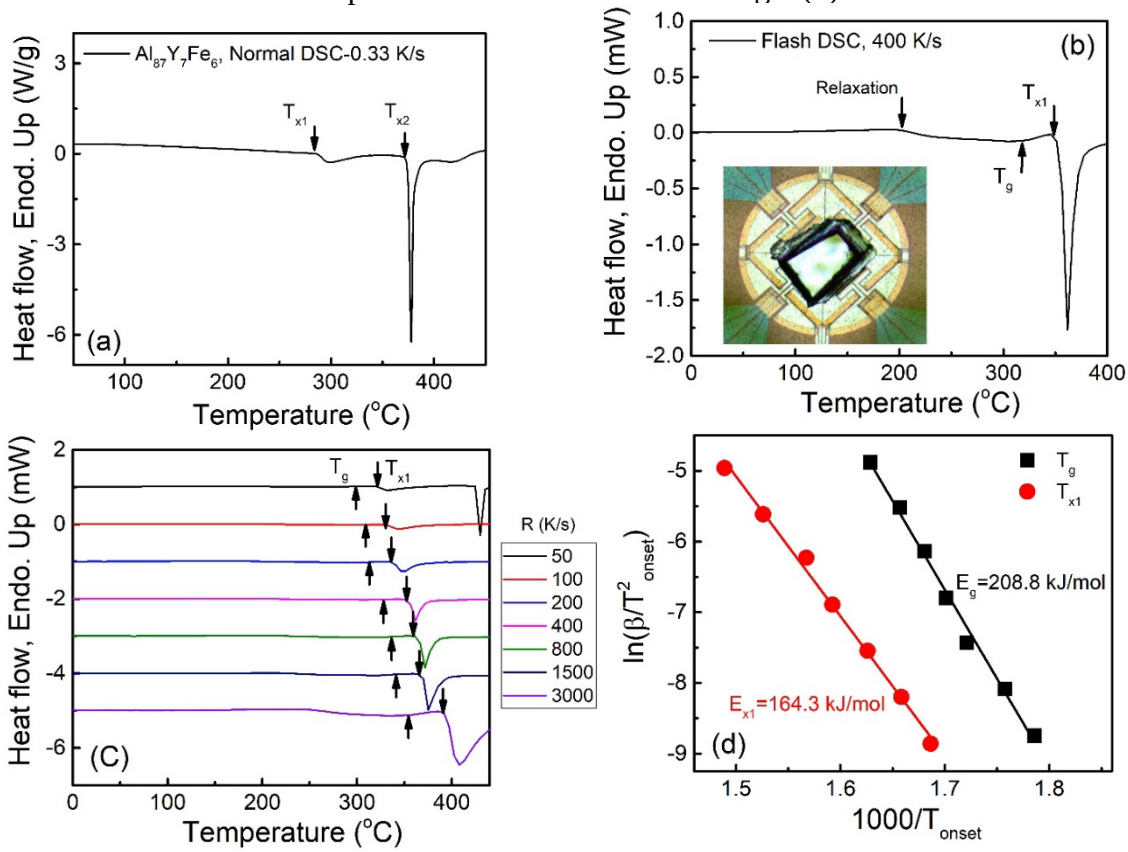

Fig. 1. (a) Conventional DSC heat flow curve for as-spun $Al_{87}Y_7Fe_6$ sample at a heating rate of 0.33 K/s. (b) Flash DSC heat flow curve at a heating rate of 400 K/s. The inserted optical picture shows the tiny sample loaded on the Flash DSC chip. (c) Experimentally measured Flash DSC heat flow curves at heating rates ranging from 50 K/s to 3000 K/s. (d) Activation energy determination for primary crystallization and glass transition by fitting T_{x1} and T_g with the Kissinger equation. The black up arrows give the onset temperature of the glass transition (T_g) and the black down arrows give the onset temperature of primary crystallization (T_{x1}).

that the Flash DSC heat flow curve exhibits both the obvious glass transition and crystallization signals. In addition, there also appears one negative step signal before the glass transition in Fig. 1(b) and this negative step is actually the structural relaxation signal. For MGs, before the glass transition (called α relaxation), there always appear a series of relaxation events, such as the β

relaxation and γ relaxation, and these relaxation events can be activated during heating and under dynamic stress [34-35]. However, by the conventional thermal analysis method with the heating rate of several K/s, the β relaxation and γ relaxation events evolve slowly and thus the obvious thermal signals originated from these relaxation events do not show up. In contrast, by the Flash DSC with maximum heating rate of 4×10^4 K/s, the different relaxation events follow different evolution paths with heating rate and then they can be easily separated from the glass transition signal under ultrafast heating rates. Thus, the negative step in Fig. 1(b) corresponds to one of the activated relaxation events at the heating rate of 400 K/s.

To further study the dynamic properties of glass transition and primary crystallization for $Al_{87}Y_7Fe_6$ MG, a series of Flash DSC heat flow curves corresponding to different heating rates temperature and the primary crystallization temperature usually follow the Kissinger equation: $\ln(\frac{\beta}{T_{onset}^2}) = (-\frac{E}{RT_{onset}}) + \text{constant}$, where β is the heating rate, T_{onset} is the value of the onset temperature of primary crystallization or the glass transition, E_g and E_{x1} are the activation energies for the glass transition and primary crystallization respectively and R is the gas constant. Thus, the activation energy for the glass transition and primary crystallization for the $Al_{87}Y_7Fe_6$ MG can be calculated by fitting the experimental results with the Kissinger equation and the detailed results are shown in Fig. 1(d). The activation energy for primary crystallization is 164.3 from 50 K/s to 3000 K/s were measured as shown in Fig. 1(c). For $Al_{87}Y_7Fe_6$ MG, the activation energy for primary crystallization is 164.3 kJ/mol and 208.8 kJ/mol for the glass transition. These activation energy values are comparable with those of previous researches in other Al-based MG systems [36-38]. Thus, for the $Al_{87}Y_7Fe_6$ MG, the glass transition requires a larger activation energy than that for the primary crystallization process. At a low heating rate in a conventional DSC, the T_g signal is superposed by the primary crystallization peak and the weak T_g signal is swallowed by the strong crystallization signal. With the increase of heating rates, both T_g and T_x move to higher temperatures. However, T_g requires more activation energy to shift, and T_g will be left behind by T_x. Therefore, it is possible to discriminate the two signals and then determine the glass transition temperature for Al-based MGs. This result is consistent with the observed glass transition in the Flash DSC heat flow curves with a series of fast heating rates in Fig. 1(c) and previous work [32].

3.1.2. Delay time confirmation based on the separation of the relaxation and composition effect

A series of Flash DSC heat flow curves at 1000 K/s for $Al_{87}Y_7Fe_6$ after different annealing treatments at 265 ˚C for different annealing times, ranging from 20 s to 6400 s, is shown in Fig. 2(a). With the increase of annealing time, the glass transition temperature shifts to higher temperature. The plot of glass transition temperature T_g with annealing time t_a at 265 ºC is shown in the middle part of Fig. 2(b). It is evident that there appears a break point at 670 s and the evolution of T_g with t_a before and after the break point follows different paths marked by two red lines with different slopes in the middle part of Fig. 2(b). For MGs, the appearance of nanocrystals in the MG matrix indicates that there exists the change of composition so that the two paths in the evolution of T_g with annealing time before and after nanocrystal appearance are separately induced by the relaxation effect and the superimposed effect of the relaxation and composition effects [32-33]. Thus, the turning point of T_g with annealing time from the relaxation effect to the superimposed effect of the relaxation and composition effects corresponds to the delay time of primary crystallization. For the other three annealing temperatures, 270 ºC, 273 ºC and 275 ºC, similar results also were obtained as shown in Fig. 2(c) and the detailed values of delay time for different temperatures are listed in the Table 1.

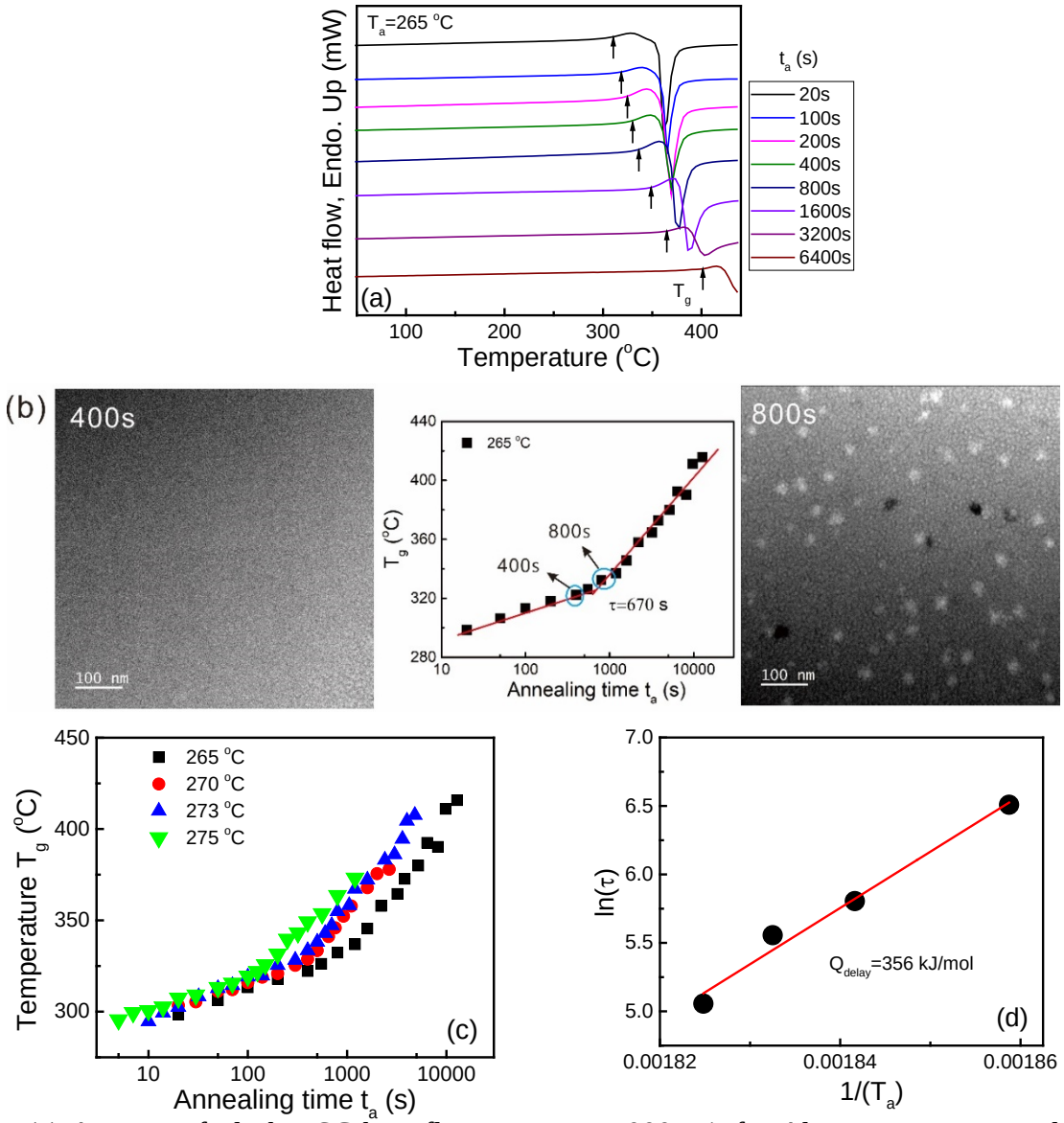

Fig. 2. (a) A series of Flash DSC heat flow curves at 1000 K/s for $Al_{87}Y_7Fe_6$ corresponding to different annealing times t_a ranging from 20 s to 6400 s at 265 °C. (b) Plot of T_g and t_a at 240 °C. T_g can be obtained from Fig. 2(a). TEM images corresponding to the samples annealed shorter (point a) and longer (point b) than the time corresponding to the break point (670 s). (c) Plot of T_g and t_a at 270 °C, 273 °C and 275 °C. (d) Delay time activation energy Q_{delay} by fitting the delay times and temperatures with the Equation (1).

To further verify if the break point of glass transition with annealing time is the delay time for primary crystallization, two annealing points at 265 °C before and after the break point were selected and the corresponding TEM images for these annealed samples are shown in the left and right parts of Fig. 2(b). These TEM samples are from the in-situ Flash DSC annealed samples and are prepared by FIB methods [39]. From Fig. 2(b), at 265 °C, the sample annealed for 400 s is still amorphous in the left micrograph of Fig. 2(b). In contrast, for the sample annealed for 800 s beyond the break point, precipitated Al-fcc nanocrystals could be detected (the right micrograph of Fig. 2b). These results confirm that the delay time measurement method based on the Flash DSC is feasible and reliable, especially for the marginal Al-based MG systems.

Prior to the appearance of the first nanocrystals there is a period of cluster evolution by fluctuational growth in cluster size space. During this period the establishment of the steady state cluster size distribution is controlled mainly by passage time (or delay time) through the random walk diffusion zone that spans the cluster sizes corresponding to formation energies within kT (k is the Boltzmann constant) of the maximum nucleation barrier [7]. Thus, if the delay time for primary crystallization is assumed to satisfy the Arrhenius relationship in the experimental temperature region [40], the temperature dependence of the delay time is given by

$$\tau = \tau_0 \exp(\frac{Q}{RT}) \quad (1)$$

where τ is the delay time, τ_0 is a constant, Q is the activation energy [40]. According to Equation (1), the experimental delay time activation energy for $Al_{87}Y_7Fe_6$ system can be well fitted in Fig. 2(d) and the value of Q_{delay} is 356 kJ/mol (3.69 eV). The diffusion coefficient activation energy value range for MGs is from 1.25 eV to 4.5 eV [41]. Therefore, the obtained delay time activation energy is 3.69 eV is within the reasonable activation energy range for MGs. While the method to measure the delay time provides a convenient and effective approach for an accurate determination, the physical significance of the activation energy derived from the Arrhenius function fit to the temperature dependence of the delay time is somewhat uncertain. As noted, the trend of T_g with annealing before the breakpoint is due to a relaxation process, but after the breakpoint the trend reflects the concurrent effects of both the relaxation and the composition change in the amorphous matrix due to nanocrystal formation. Due to the operation of multiple processes, the Q value is best regarded as an effective activation energy. At the same time, it will be shown that the effective Q can still be useful in providing guidance in the design of alloy compositions with enhanced glass formation ability.

3.2. Cu-minor alloying effect on the delay time for $Al_{88}Y_7Fe_5$ MGs

For Al-based MGs, both the crystallization behaviors and glass formation ability are very sensitive to minor element substitution and the underlying mechanism has been studied in terms of the structural, thermodynamic and kinetic factors [9-13, 38, 40, 42]. However, considering the difficulty in the precise measurement of the delay time, there are few studies focusing on the minor alloying effect on the transient nucleation, especially for the delay time of primary crystallization of nanocrystal Al precipitation [23]. In Fig. 3, the DSC heat flow curves for every component substitution by Cu at 20 K/min were measured and the results are listed in Table 1. It

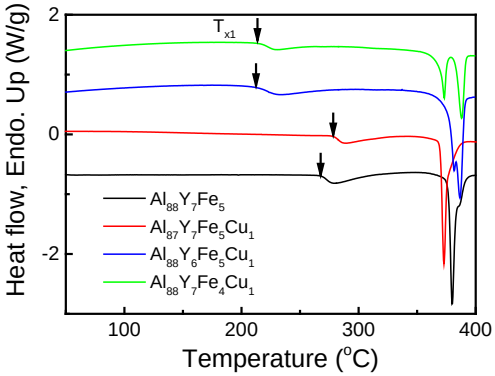

Fig. 3. Heat flow curves by normal DSC at 20 K/min for 1 at.% Cu-alloying in $Al_{88}Y_7Fe_5$ systems. The down black arrows point to the onset temperature of primary crystallization.

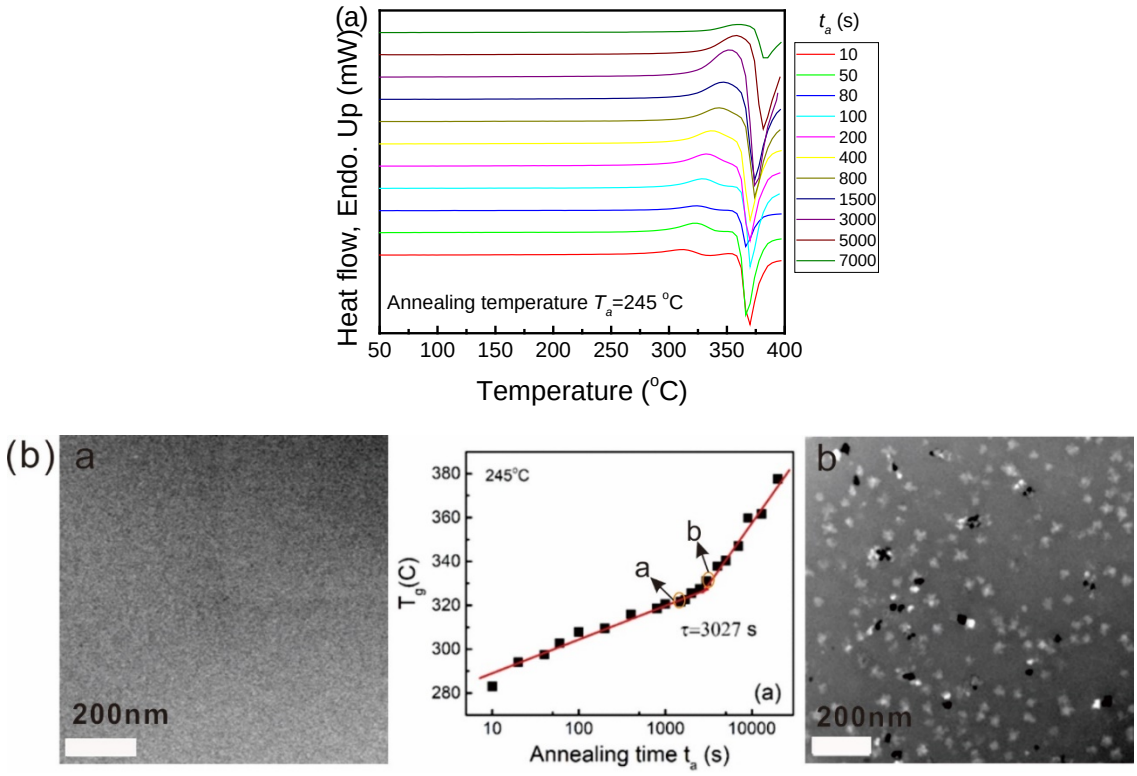

Fig. 4. (a) A series of Flash DSC heat flow curves at 1000 K/s for $Al_{87}Y_7Fe_5Cu_1$ corresponding to different annealing times t_a ranging from 10 s to 7000 s at 245 °C. (b) (Middle) T_g versus $logt_a$ plot for $Al_{87}Y_7Fe_5Cu_1$ at 245 °C. TEM images were taken for $Al_{87}Y_7Fe_5Cu_1$ samples annealed for shorter (2000 s, left micrograph) and longer (4000 s, right micrograph) than the time corresponding to the break point (3027 s) at 245 °C.

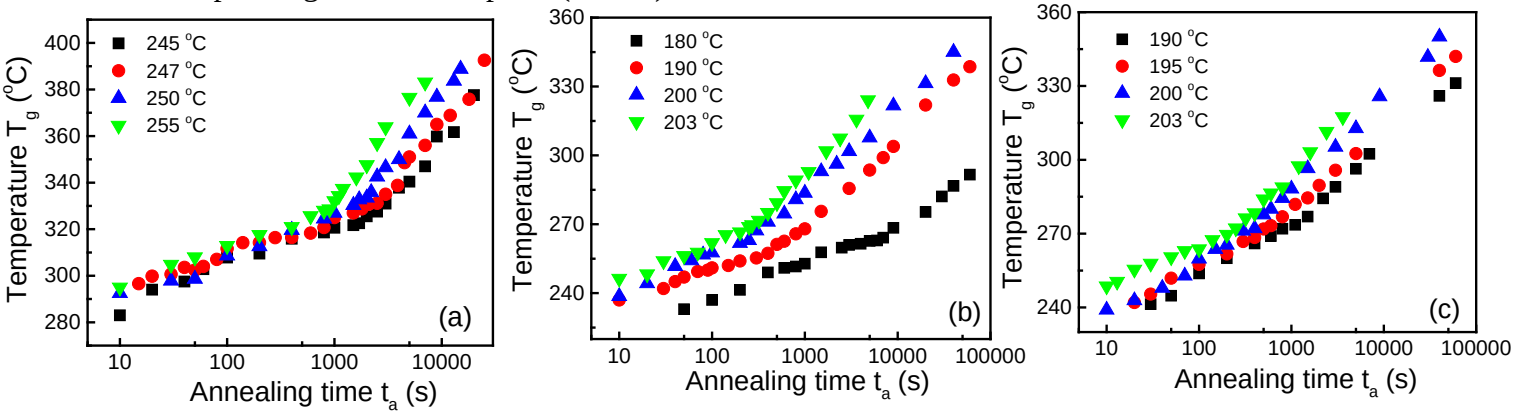

Fig. 5. T_g versus $logt_a$ plot for Cu-alloying in $Al_{88}Y_7Fe_5$ alloys at different T_a: (a) $Al_{87}Y_7Fe_5Cu_1$, (b) $Al_{88}Y_6Fe_5Cu_1$, (c) $Al_{88}Y_7Fe_4Cu_1$.

is evident that a 1 at.% replacement of Al, Y and Fe in $Al_{88}Y_7Fe_5$ by Cu induces a large change for the primary crystallization temperature. Replacements of Y and Fe by Cu leads to a 46 °C and 45 °C decrease of T_{x1} respectively, but the replacement of Al by Cu yields an increase in T_{x1} of

11 ^{o}C. This result indicates the substitution of 1 at.% of Al by Cu in the $Al_{88}Y_7Fe_5$ amorphous alloy delays the onset of primary crystallization, but the replacement of Y and Fe by Cu significantly promotes the primary crystallization by reducing the primary crystallization onset temperature. Since the Cu substitution at the 1% level will have a negligible effect on the thermodynamic driving free energy for nucleation and any change in the glass/crystal interfacial energy due to Cu segregation should be independent of the substituted component, these parameters will not account for the significant changes in the observed primary crystallization onset temperatures. However, since the crystallization onset temperature is sensitive to the delay time, it is necessary to study the delay time evolution with minor alloying in order to investigate the physical mechanism of the minor alloying effect on nucleation and crystallization. In Fig. 4, the delay time for $Al_{87}Y_7Fe_6$ MG has been confirmed. To determine if the Cu element doping affects the delay time, the $Al_{87}Y_7Fe_5Cu_1$ alloy was selected and the similar experimental method was used to measure the evolution of T_g with t_a at 245 ^{o}C. The detailed results for T_g with t_a are shown in Fig. 4(a) and 4(b). Once again, there appears one break point in the plot of T_g and t_a at 245 ^{o}C and this break point actually corresponds to the delay time of primary crystallization confirmed by TEM results shown in Fig. 4(b). Similarly, based on the above Flash DSC method, the delay times for $Al_{87}Y_7Fe_5Cu_1$, $Al_{88}Y_6Fe_5Cu_1$ and $Al_{88}Y_7Fe_4Cu_1$ corresponding to four different annealing temperatures were measured, as shown in Fig. 5(a)-5(c). The detailed values of delay time for every composition are listed in Table 1 along with the delay time for $Al_{88}Y_7Fe_5$ [32]. For every case of component substitution by Cu, there always appears one break point which is similar to the results for

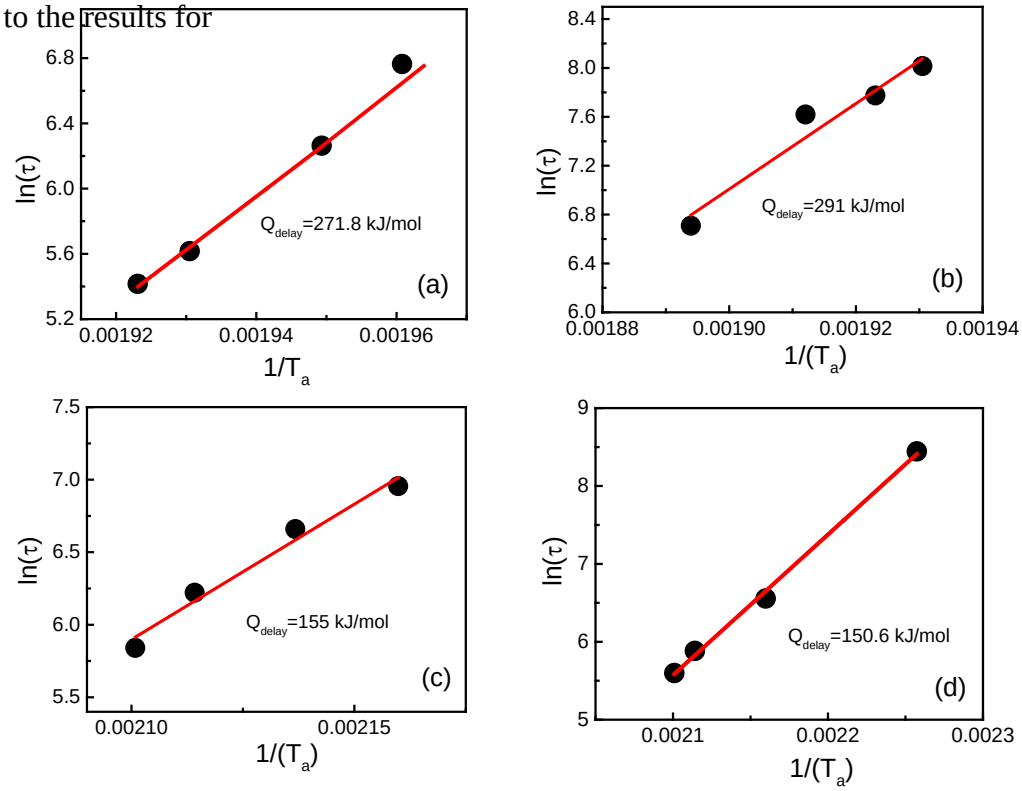

Fig. 6. Delay time activation energy Q_{delay} by fitting the Equation (1) for: (a) $Al_{88}Y_7Fe_5$; (b) $Al_{87}Y_7Fe_5Cu_1$; (c) $Al_{88}Y_6Fe_5Cu_1$; (d) $Al_{88}Y_7Fe_4Cu_1$.

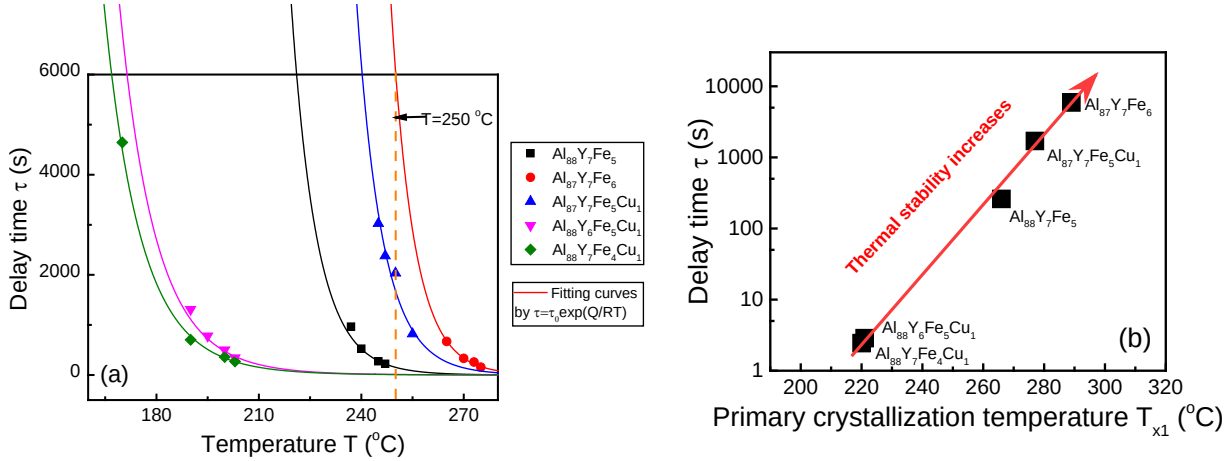

Fig. 7. (a) Plot of delay time vs. temperature for $Al_{88}Y_7Fe_5$, $Al_{87}Y_7Fe_6$, $Al_{87}Y_7Fe_5Cu_1$, $Al_{88}Y_6Fe_5Cu_1$ and $Al_{88}Y_7Fe_4Cu_1$. The orange dashed line gives the isothermal line at 250 °C and is used to confirm the delay time at 250 °C. (b) Delay time at 250 °C and the primary crystallization temperature for $Al_{88}Y_7Fe_5$, $Al_{87}Y_7Fe_6$, $Al_{87}Y_7Fe_5Cu_1$, $Al_{88}Y_6Fe_5Cu_1$ and $Al_{88}Y_7Fe_4Cu_1$. The red arrowed curve gives the evolution of the delay time with the primary crystallization temperature for different compositions.

$Al_{87}Y_7Fe_6$. With the increase of annealing temperature, the break point shifts to the shorter time and a higher annealing temperature accelerates the primary crystallization. The temperature dependence of the experimental delay time for Cu substitution in all alloys can be well fitted by equation (1) as shown in Fig. 6. The detailed values of Q_{delay} are listed in Table 2. It is remarkable that only a 1 at.% substitution by Cu in $Al_{88}Y_7Fe_5$ induces a large change for Q_{delay}. To more quantitatively compare the Cu substitution effect on the delay time for primary crystallization in $Al_{88}Y_7Fe_5$ systems, the values of the delay time at 250 °C for all AlYFe alloys were derived from Fig. 7(a) and are plotted in Fig. 7(b). The results indicate that the replacement of Y and Fe by Cu 1decreases the primary crystallization temperature and delay time, and thus reduces the thermal stability. In contrast, the replacement of Al by Cu increases the primary crystallization and delay time, and thus enhances the thermal stability, as shown in Fig. 7(b). Thus, the delay time can provide one quantitative characterization parameter to investigate the metallic glass stability against crystallization.

3.2.2. Minor-alloying effect on the glass formation ability of the $Al_{88}Y_7Fe_5$ MG

Based on the above results, different 1 at.% Cu substitutions have a big influence on the delay time τ and the delay time activation energy Q_{delay}. The delay time stands for the time for new crystalline detection in a system and an extension of the delay time indicates a higher level of crystallization resistance. Meanwhile, the delay time activation energy may be related to the diffusion behavior [40]. Thus, there should exist a positive correlation between the delay time activation energy and glass formation ability. To verify this correlation, the three Cu substitution compositions and

$Al_{88}Y_7Fe_5$ were examined to determine the critical wheel speed for glass formation during melt spinning. For every composition, a series of ribbons with different wheel speeds were produced from the same ingot and then were examined by XRD to confirm the minimum value of the wheel speed to yield a fully amorphous sample. Fig. 8(a) shows the confirmation of the critical wheel speed for $Al_{88}Y_7Fe_5$, which is between 10 m/s and 15 m/s.

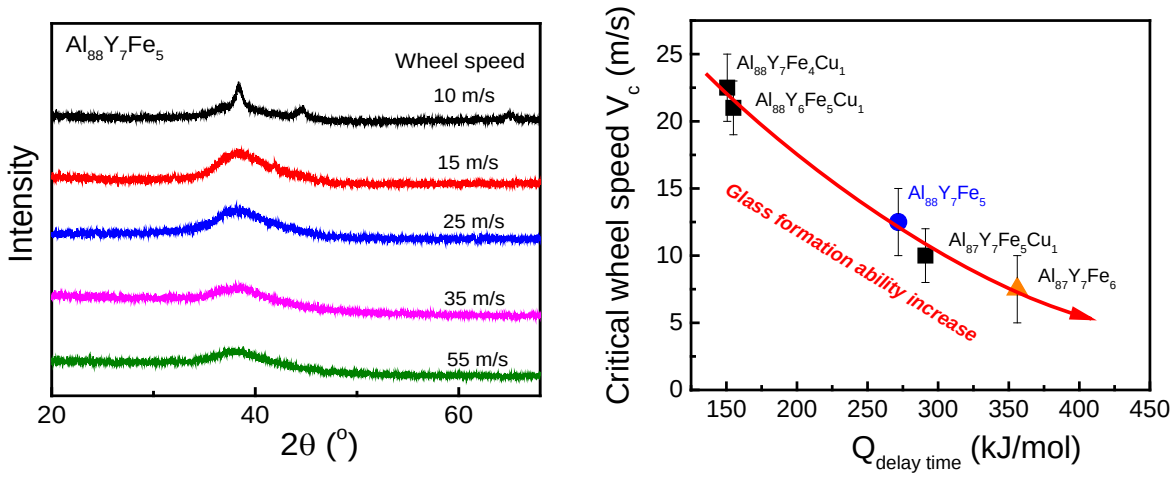

Fig. 8. (a) XRD curves corresponding to different melt-spinning wheel speeds for $Al_{88}Y_7Fe_5$. (b) The plot of critical wheel speed for glass formation and the delay time activation energy for five different compositions.

Composition	Temperature T_a (°C)	Delay time τ (s)
$Al_{88}Y_7Fe_5$	237	966
	240	525
	245	275
	247	225
$Al_{87}Y_7Fe_6$	265	670
	270	332
	273	258
	275	157
$Al_{87}Y_7Fe_5Cu_1$	245	3027
	247	2380
	250	2036
	255	820
$Al_{88}Y_6Fe_5Cu_1$	190	1312
	195	780
	200	503
	203	344
$Al_{88}Y_7Fe_4Cu_1$	170	4645
	190	703

	200	359
	203	270

Table 1. Delay time τ for different annealing temperatures, T_a for minor alloying in $Al_{88}Y_7Fe_5$.

Similarly, for other compositions, the values of the critical wheel speed were also obtained and are listed in Table 2. The relationship between the critical wheel speed and the delay time activation energy can be plotted in the Fig. 8(b). From this plot, it is apparent that the delay time activation energy has a positive correlation with the glass formation ability. With the increase of

Composition	**T_{x1} (°C)**	**T_{x2} (°C)**	**Q_{delay} (kJ/mol)**	**$T_{m\text{-doping element}} \rightarrow T_{m\text{-substituted element}}$ (°C)**	**V_c (m/s)**
$Al_{88}Y_7Fe_5$	266	373	271.8	--	13±3
$Al_{87}Y_7Fe_6$	289↑	375↑	356↑	660→1538	8±2
$Al_{87}Y_7Fe_5Cu_1$	277↑	369↓	291↑	660→1085	10±2
$Al_{88}Y_6Fe_5Cu_1$	220↓	375↑	155↓	1526→1085	21±3
$Al_{87}Y_7Fe_4Cu_1$	221↓	365↓	150.6↓	1538→1085	23±3

Table 2. Summary of thermodynamic and kinetic properties for different Cu alloying compositions in $Al_{88}Y_7Fe_5$. The black up and down arrows give the increasing and decreasing trends compared to the values for $Al_{88}Y_7Fe_5$.

delay time activation energy, the critical wheel speed decreases and there is an enhancement in the glass formation ability.

To further investigate the relationship between the minor-alloying substitution and the glass formation ability, the melting temperature change of the minor-alloying elements and the replaced elements for all systems examined in this work are listed in Table 2. It is interesting to observe that for all minor alloying substitutions, when the melting temperature of the minor alloying element is larger than that for the substituted element, the primary crystallization temperature and the delay time activation energy increase and when the melting temperature of the minor alloying element is smaller than that for the substituted Al element, the primary temperature and the delay time activation energy decrease. Moreover, the larger the melting temperature difference between the minor alloying element and the substituent element, the larger is the change of T_{x1} and Q_{delay}. These results may provide a criterion for developing novel Al-based amorphous alloys with high thermal stability and glass formation ability based upon minor alloying with high melting

temperature elements. For example, to illustrate this criterion, the critical wheel speed for glass formation in $Al_{88}Y_7Fe_5$ can be compared with that of $Al_{87}Y_7Fe_6$ where a 1 at.% Fe has replaced Al. Since Fe with higher melting temperature replaces the Al, both the delay time activation energy and the glass formation ability should increase. From Fig. 8(b), the experimental results are consistent with the above deduction. These results are also consistent with the previous minor-alloying research in Al-based MGs [9-10].

4. Conclusion

In conclusion, a novel method to precisely measure the delay time of primary crystallization based on the ultrafast Flash DSC has been established in Al-based MGs and applied to examine the effect of minor alloying. By Flash DSC, for marginal Al-based MGs, the primary crystallization temperature for Al nanocrystal precipitation and the glass transition are separated successfully at high heating rate. By analyzing the evolution of the glass transition temperature with annealing time, a break point appears resulting from a transition from the relaxation effect to the composition and relaxation effect. TEM results before and after the break point demonstrate that the Al nanocrystals cannot be detected until the annealing time exceeds the break point time. Thus, the break point time corresponds to the delay time of primary crystallization. Since the method to evaluate the delay time relies on the change in amorphous matrix composition that leads to a change in the annealing response of T_g, it is expected to apply to other MGs that undergo primary crystallization as the first reaction during devitrifiation. To extend the method application, the effect of a series of component substitutions by Cu was studied on the delay time in an $Al_{88}Y_7Fe_5$ base alloy. The significant changes in the primary crystallization onset temperature due to the Cu substitution are demonstrated to be directly related to the corresponding changes in the delay time. The results indicate that minor alloying that is designed to increase the delay time is an effective strategy to enhance glass formation ability.

References

[1] A.L. Greer, Crystallization of metallic glasses, Mater. Sci. Eng. A 179 (1994) 41-45.

[2] R. Busch, J. Schroers, W.H. Wang, Thermodynamics and kinetics of bulk metallic glass, MRS Bulletin 32 (2007) 620-623.

[3] W.L. Johnson, Bulk glass-forming metallic alloys: Science and technology, MRS Bulletin 24 (1999) 42-56.

[4] K.F. Kelton, A.L. Greer, Transient nucleation effects in glass formation, J. Non-Cryst. Solids 79 (1986) 295-309.

[5] V.M. Fokin, A.M. Kalinina, V.N. Filipovich, Nucleation in silicate glasses and effect of preliminary heat treatment on it, J. Cryst. Growth 52 (1981) 115-121.

[6] V.M. Fokin, E.D. Zanotto, N.S. Yuritsyn, J.W.P. Schmelzer, Homogeneous crystal nucleation in silicate glasses: A 40 years perspective, J. Non-Cryst. Solids 352 (2006) 2681-2714.

[7] H.I. Aaroson, J.K. Lee, The kinetic equations of solid-solid nucleation theory, Lectures on the Theory of Phase Transformations, New York: The Metallurgical Society of AIME, 1975, pp. 83-115.

[8] Z.P. Lu, C.T. Liu, A new glass-forming ability criterion for bulk metallic glasses, Acta Materialia 50 (2002) 3501–3512.

[9] K.S. Bondi, A.K. Gangopadhyay, Z. Marine, T.H. Kim, A. Mukhopadhyay, A.I. Goldman, W.E. Buhro, K.F. Kelton, Effects of microalloying with 3d transition metals on glass formation in AlYFe alloys, J. Non-cryst. Solids 353 (2007) 4723–4731.

[10] A. Mukhopadhyay, K.E. Spence, L.Q. Xing, W.E. Buhro, K.F. Kelton, An Al-rich metallic glass with a large supercooled liquid region, Philos. Mag. 2 (2007) 281-290.

[11] Y. Shen, J.H. Perepezko, Al-based amorphous alloys: Glass-forming ability, crystallization behavior and effects of minor alloying additions, J. Alloy. Compd. 707 (2017) 3-11.

[12] W. Zhang, S.Q. Chen, Z.W. Zhu, H.Wang, Y.H. Li, H. Kato, H.F. Zhang, Effect of substituting elements on thermal stability and glass-forming ability of an Al-based Al-Ni-Er metallic glass, J. Alloy. Compd. 707 (2017) 97-101.

[13] N.C. Wu, L. Zuo, J.Q. Wang, E. Ma, Designing aluminum-rich bulk metallic glasses via electronic-structure-guided microalloying, Acta Mater. 108 (2016) 143-151.

[14] Y.T. Zhu, T.C. Lowe, R.J. Asaro, Assessment of the theoretical basis of the Rule of Additivity for the nucleation incubation time during continuous cooling, J. Appl. Phys. 82 (1997) 1129-1137.

[15] D.T. Wu, The time lag in nucleation theory, J. Chem. Phys. 97 (1992) 2644-2650.

[16] K.F. Kelton, Time-dependent nucleation in partitioning transformation, Acta Mater. 48 (2000) 1967-1980.

[17] J.H. Perepezko, S.D. Imhoff, Primary crystallization reactions in Al-based metallic glass alloys, J. Alloy. Compd. 504 (2010) 222-225.

[18] B. Zhang, D.Q. Zhao, M.X. Pan, W.H. Wang, A.L. Greer, Amorphous Metallic Plastic, Phys. Rev. Lett. 94 (2005) 205502.

[19] W.L. Johnson, Fundamental aspects of bulk metallic glass formation in multicomponent alloys, in Materials Science Forum, 1996, Trans Tech Publ.

[20] R.I.I. Wu, Doctoral thesis (2001), University of Wisconsin-Madison.

[21] Y. Shen, J.H. Perepezko, The effect of minor addition of insoluble elements on transformation kinetics in amorphous Al alloys, J. Alloys. Compd. 643 (2015) S260-S264.

[22] L.Q. Xing, A. Mukhopadhyay, W.E. Buhro, K.F. Kelton, Improved Al-Y-Fe glass formation by microalloying with Ti, Philos. Mag. Lett. 84 (2004) 293-302.

[23] J. Deubener, R. Briickner, M. Sternitzke, Induction time analysis of nucleation and crystal growth in di- and metasilicate glasses, J. Non-Cryst. Solids 163 (1993) 1-12.

[24] A.I. Taub, F. Spaepen, The kinetics of structural relaxation of a metallic glass, Acta Metall. 28 (1980) 1781-1788.

[25] C. Moynihan, P.B. Macedo, C.J. Montrose, C.J. Montrose, P.K. Gupta, M.A. DeBolt, J.F. Dill, B.E. Dom, P.W. Drake, A.J. Easteal, P.B. Elterman, R.P. Moeller, H. Sasabe, J.A. Wilder, Structural Relaxation in Vitreous Materials, Ann. N. Y. Acad. Sci. 279 (1976) 15-35.

[26] I.M. Hodge, Enthalpy relaxation and recovery in amorphous materials, J. Non-Cryst. Solids 169 (1994) 211-266.

[27] G.P. Johari, J.G. Shim, Enthalpy recovery on thermal cycling within the non-equilibrium state of a glass, J. Non-Cryst. Solids 261 (2000) 52-66.

[28] A. Inoue, T. Masumoto, H.S. Chen, Enthalpy relaxation behaviour of (Fe, Co, Ni)75Si10B15 amorphous alloys upon low temperature annealing, J. Mater. Sci. 19 (1984) 3953-3966.

[29] M.D. Ediger, C.A. Angell, S.R. Nagel, Supercooled Liquids and Glasses, J. Phys. Chem. 100 (1996) 13200-13212.

[30] E. Zhuravlev, C. Schick, Fast scanning power compensated differential scanning nano-calorimeter: 1. The device, Thermochim. Acta 505 (2010) 1-13.

[31] E. Zhuravlev, C. Schick, Fast scanning power compensated differential scanning nano-calorimeter: 2. Heat capacity analysis, Thermochim. Acta 505 (2010) 14-21.

[32] Y. Shen, J.H. Perepezko, Investigation of the Nucleation Delay Time in Al-based Metallic Glasses by the High Rate Calorimetry, J. Non-Cryst. Solids 502 (2018) 9-14.

[33] Y. Shen, Doctoral thesis (2016), University of Wisconsin-Madison.

[34] H.S. Chen, E. Coleman, Structural relaxation spectrum of metallic glasses, Appl. Phys. Lett. 28 (1976) 245-247.

[35] H.B. Yu, W.H. Wang, H.Y. Bai, K. Samwer, The β relaxation in metallic glasses, Natl. Sci. Rev. 1 (2014) 429-461

[36] A. Inoue, N. Matsumoto, T. Masumoto, Al–Ni–Y–Co Amorphous Alloys with High Mechanical Strengths, Wide Supercooled Liquid Region and Large Glass-Forming Capacity, Mater. Trans. JIM 31 (1990) 493-500.

[37] F. Ye, K. Lu, Crystallization kinetics of Al–La–Ni amorphous alloy, J. Non-Cryst. Solids 262 (2000) 228-235.

[38] J.Q. Wang, Y.H. Liu, S. Imhoff, N. Chen, D.V. Louzguine-Luzgin, A. Takeuchi, M.W. Chen, H. Kato, J.H. Perepezko, A. Inoue, Enhance the thermal stability and glass forming ability of Al-based metallic glass by Ca minor-alloying, Intermetallics 29 (2012) 35-40.

[39] P. Zhang, J.H. Perepezko, P.M. Voyles, Elastic and inelastic mean free paths of 200 keV electrons in metallic glasses, Ultramicroscopy 171 (2016) 89-95.

[40] D.M. Herlach, D.M. Matson, Solidification of Containerless Undercooled Melts, Weinheim, Germany: Wiley-VCH Verlag GmbH & Co. KGaA, 2012, pp. 87-111.

[41] F. Faupel, W. Frank, M.-P. Macht, H. Mehrer, V. Naundorf, K. Rätzke, H.R. Schober, S.K. Sharma, H. Teichler, Diffusion in metallic glasses and supercooled melts, Rev. Mod. Phys. 75 (2003) 237-280.

[42] Y. Shen, J.H. Perepezko, Al-based amorphous alloys: Glass-forming ability, crystallization behavior and effects of minor alloying additions, J. Alloys Compd. 707 (2017) 3-11.

Part II

Al-based amorphous metallic plastics

1.Introduction

Polymeric glasses have a very wide range of applicability because they exhibit the good thermoplastic deformation ability arising from their high glass-forming ability (GFA), low glass transition temperature, and large supercooled liquid region [1–3]. The thermoplastic nature of common glassy polymers is exploited in molding and imprinting. For metallic glasses (MGs), the exceptional processing ability and large supercooled liquid region enable them as promising candidates for thermoplastic processing [4-6]. This processing opportunity has been used for a wide range of applications, including net-shape processing [7-8], micro- and nano-replication [9-10], extrusion [11], synthesis of amorphous metallic foams [12], superplastic forming of sheet materials [13], and synthesis of MG composites [14]. However, these MGs systems, such as Zr-, Ti-, Fe- and Ni-based, usually exhibit a high glass transition temperature T_g, which largely limits the development and applications at low temperature range. Meanwhile, a series of new MGs with exceedingly low glass transition temperature T_g, amorphous metallic plastics, were recently developed, such as the Ce-, Ca-, Sr- and La-based amorphous systems [15-18]. At low temperature (near or lower than the boiling water temperature), these amorphous metallic plastics can easily realize the thermoplastic deformation, such as mechanical deformation and imprinting [15-16]. However, these MGs with a low T_g are usually highly unstable to crystallization [19]. Specially, considering that these amorphous metallic plastics are the rare-earth element systems, the oxidation resistance and the corrosion resistance are very poor, and the materials cost is relatively high in view of these scarce rare-earth elements. Therefore, one new amorphous metallic plastic with low cost and good corrosion resistance is desirable.

Al-based MGs have attracted increasing attentions for decades due to their outstanding properties, such as high specific strength, high elastic strain limit and good corrosion resistance [20]. Due to the relative low glass forming abilities (GFAs), previous investigations mainly focused on the GFAs, thermal stability and crystallization behavior of Al-based MGs [21-22]. According to the elastic modulus criterion of composition elements and the positive relationship between the elastic modulus and glass transition in MGs [23], Al-based MGs with low-melting alloying elements should have the lower glass transition temperature. For most of MG systems, the glass transition signal is strong enough to show up in the heating DSC trace, which makes it possible to measure the glass transition temperature and the supercooled liquid zone by normal DSC method. However, for marginal Al-based MGs, the glass transition signal is prone to be covered by a primary nucleation peak for Al nanocrystals followed by secondary or tertiary crystallization reactions involving intermetallic phases [24]. Thus, the traditional DSC is not a

good thermal method to observe the glass transition behaviors of Al-based MGs. Recently, Y. Shen *el at.* applied the advanced Flash DSC with ultrafast heating and cooling rate to successfully separate the glass transition and primary crystallization signals of AlYFe MG system [25], which provides an opportunity to study the kinetic behaviors in the supercooled liquid zone and the thermoplastic deformation ability for Al-based MGs.

In this work, we developed a family of AlSm-based MGs (MGs), which exhibit polymerlike thermoplastic formability near water boiling point (100^{o}C). By the advanced Flash DSC, the glass transition signals with different heating rates for AlSm-based MG systems were observed and we found that the glass transition temperatures for these AlSm-based MGs are below than the boiling point of water. Then we designed a simple experiment to further confirm that these Al-based MGs own the thermoplastic deformation ability near water boiling point. By comparing the supercooled liquid zone and the crystallization activation energy, the $Al_{90}Sm_8Ag_2$ MG has highest thermal stability, which is the ideal candidate to realize the thermoplastic processing. To further verify the thermoplastic processing ability for the $Al_{90}Sm_8Ag_2$ MG, the implantation test was conducted and a "UW" mark was successfully implanted on the surface in the boiling water.

2.Experimental details

All ingots following the compositions of $Al_{92}Sm_8$, $Al_{91}Sm_8Cu_1$, $Al_{91}Sm_8Cu_2$, $Al_{91}Sm_8Ag_1$ and $Al_{91}Sm_8Ag_2$ (at.%) were produced by arc melting of pure components for at least five times to ensure homogeneity. The chemical compositions for the ingots were confirmed by Energy Dispersive Analysis (EDS, scanning electron microscope LEO 1530). A series of ribbons for the above compositions were formed by single roller melt spinning on a copper wheel with tangential speeds of 55m/s. Both arc melting and melt spinning were performed in an inert argon atmosphere. The glassy nature of the as-spun ribbons was ascertained by X-ray diffraction (Bruker D8 Discover Diffraction with Cu K_α radiation), as were shown in Fig. 1(a). A PerkinElmer Diamond DSC was used to characterize the thermodynamic properties with a heating rate 20 K/min in Fig.1(b).

3.Results and discussion

From Fig. 1(b), one can clearly see that there is no glass transition signal in all heat flow curves and the primary crystallization corresponding to the precipitation of Al nanocrystals [26] firstly appears in all AlSm-based samples marked by black arrows. The onset temperatures T_{x1} for the primary crystallization and T_{x2} for the secondary crystallization for these AlSm-based systems are listed in the Table 1.

Considering that the glass transition and crystallization are significantly different dynamic processes and there are different evolution paths with heating, these two dynamic signals should be separated under higher heating rate. For normal DSC, the measurement range of heating rate is extremely limited. In contrast, for Flash DSC, the maximum heating rate can reach to $4*10^4$ K/s, which is the powerful tool to separate the different dynamic processes. Thus, based on the above idea, we first cut the melt-spun ribbon into small pieces of approximately 0.16 mm×0.16 mm under an optical microscope and then loaded the tiny sample piece on the chip by a hair pen of the Flash DSC (Flash DSC 1, Mettler Toledo), as is shown in the inserted picture of Fig. 1(c). From the insertion of Fig. 1(c), a typical Flash DSC heat flow curve with heating rate of 1000K/s for $Al_{92}Sm_8$ was measured. At low temperature (around 190˚C), an exothermic relaxation signal is manifested, followed by an endothermic glass transition signal T_g (around 200˚C) and a sharp

primary crystallization peak of Al_{fcc} nanocrystals (around 240˚C). Similarly, the heat flow curves corresponding to various heating rates for $Al_{92}Sm_8$ were obtained and are shown in the Fig. 2. Based on these heat flow curves, the detailed values of T_g corresponding to different heating rates were obtained. For MGs, the dynamic evolution behavior of glass transition with heating rate can be well described by the Kissinger equation [27]. Thus, the glass transition temperature T_g at lower heating rate of 20K/min (0.33K/s) can be estimated by extrapolating the Kissinger equation into 0.33K/s in Fig. 1(c) and the value of T_g is about 90^{o}C. In the same way, the values of T_g for other AlSm-based systems can also be obtained (The detailed heat flow curves and the Kissinger plots were shown in the Fig. 3) and the values of T_g are listed in Table 1. Surprisingly, as is shown in Fig. 1(d), the glass transition temperatures for all AlSm systems are very close to that of some common amorphous polymers, such as polyvinylchloride (75–105 ^{o}C) [28] and are lower than the boiling point of water (100^{o}C).

To further verify the glass transition temperature obtained by the above extrapolating method based on the Flash DSC, we measured the viscosity η evolution with temperature for $Al_{92}Sm_8$ ribbon based on the vibrational loading method [29]. For liquids, upon cooling below the freezing point, molecular motion slows down, and the molecules gradually arrange in the periodical order to form crystal. If the liquid is cooled sufficiently fast, molecules will rearrange so slowly that they cannot adequately sample configurations in the available time allowed by the cooling rate and crystallization can be avoided. The liquid's structure therefore appears 'frozen' on the laboratory and the resulting material is a glass. The slower a liquid is cooled, the longer the time available for configurational sampling at each temperature, and hence the colder it can become before falling out of liquid-state equilibrium. Consequently, T_g increases with cooling rate. In practice, the dependence of T_g on the cooling rate is weak (T_g changes by 3–5 °C when the cooling rate changes by an order of magnitude [30]), and the transformation range is narrow, so that T_g is an important material characteristic. Thus, we can use DSC method to measure the T_g. Meanwhile, another definition of T_g is the temperature at which the shear viscosity reaches 10^{12} Pas. When the temperature is close to T_g, the viscosity η is extraordinarily sensitive to temperature and different glassy materials exhibit different dynamic behaviors, which can be described by fragility in the Angell plot [30]. Thus, we can evaluate the T_g value based on the viscosity evolution with temperature. Here, we took the $Al_{92}Sm_8$ MG as an example. To estimate the evolution of viscosity with temperature for $Al_{92}Sm_8$ MG, we applied Dynamic Mechanical Analyzer (DMA) RSA III to perform the vibrational loading experiments [29]. The detailed experimental parameters and sample information are seen in the insertion of Fig. 4(a). In Fig. 4(a) and 4(b), the displacement–temperature (time) and stress-temperature (time) curves were derived from the original DMA results. From Fig. 4(a), the strain rate ($\dot{\varepsilon}$)–temperature (T) curves can be deduced from the above displacement (D)–time (t) curves according to the definition $\dot{\varepsilon}=\dot{D}/D_0$ (Fig. 4(c)), where D and D_0 denote the displacement and the original length of the MG ribbon sample, respectively. Then, the apparent viscosities (η) can be determined according to the equation, $\eta=\sigma/3\dot{\varepsilon}$ and the viscosity evolution with the reduced temperature (T_g/T, T_g=90^{o}C) is shown in Fig. 4(d). It can be clearly seen that the viscosity is about $(1.3\pm0.3)\times10^{12}$ Pas when the temperature approaches to the glass transition temperature (T_g=90^{o}C, T_g/T=1) and it is consistent with the second definition of glass transition temperature, which verifies the validity of our method based on the Flash DSC.

The AlSm-based MG systems in this work actually display a low glass transition temperature that is close to the boiling point of water, which provides the prerequisite for the applications based

on the thermoplastic deformation in the supercooled liquid zone. The molding and imprinting previously reported for oxide glasses and conventional MGs have had to be performed at higher temperatures [31-32]. For oxide glasses, for example, T_g~700 °C; and for Zr-based MGs, T_g~350°C [31], and for Ti-, Fe-, and Cu-based MGs, T_g is even higher [32]. Because of the high T_g, molding of MGs is often performed as part of the original quench, in a squeezing-casting or high-pressure casting process. To investigate the thermoplastic deformation of AlSm-based MGs, a series of simple comparison tests were conducted, and the experimental setup is shown in Fig. 5(a). Two ribbon pieces with equal width and length were cut from one ribbon and were bent to the same curvature by a tweezer. Then, these two curving MG pieces were respectively placed at room temperature and in the boiling water (about 100^{o}C) for 30 seconds (see in the left and right part of Fig. 5(a)) and then released. The left and right pictures in Fig. 5(b)-5(f) display the morphology of two ribbon pieces after releasing for five AlSm-based MG ribbons at room temperature and in boiling water, respectively. One can clearly see that the ribbon pieces at room temperature still kept the original shape for all AlSm systems; in contrast, the permanent deformation happened for the ribbon pieces being placed in boiling water. By magnifying the microscopic regions with maximum curvature of the above deformed pieces in the boiling water, there exist no shear bands for all deformed pieces in the right SEM images of Fig. 5(b)-5(f) (marked by red dashed circles and lines), which indicates that the permanent deformation is the thermoplastic deformation rather than the plastic deformation dependent on the formation and development of multiple shear bands [33]. Therefore, the above contrast tests reveal that the AlSm systems with low glass transition temperature exhibit the thermoplastic deformation ability near the boiling point of water. Moreover, it should be noted that it is easy to oxidize and corrode the Ce-, Ca-, Sr- and La-based amorphous systems as previously reported [15-18]. For AlSm MG systems in this work, the surfaces remained as shiny as the as-cast state after deforming in the boiling water and the micro-regions did not display an oxidation scale, which implies a good corrosion resistance.

For MG systems, the large supercooled liquid region ΔT and the high crystallization activation energy E_{x1} indicate higher thermodynamic stability of their supercooled liquid state [31]. Based on the heat flow curves with different heating rate for every system, we calculated the ΔT and the E_{x1} by fitting the Kissinger equation for all AlSm-based MG systems and the detailed results are listed in the Table 1. The plot of ΔT and E_{x1} for the AlSm-based systems is shown in Fig. 6(a). Obviously, the MG system of $Al_{90}Sm_8Ag_2$ lying in the top right corner marked by red dashed circle in Fig. 6(a) should have the strongest thermal stability in these AlSm-based MGs, which should be the best candidate for thermoplastic applications. To further investigate the thermal stability of $Al_{90}Sm_8Ag_2$ MG sample, the time-temperature-transformation (TTT) diagram at low temperature was determined in Fig. 6 (b). For MGs, the TTT diagram is usually measured by the isothermal experiments. The samples are annealed at one temperature and the isothermal crystallization of the alloy is investigated by XRD. However, for Al-based MGs, there is a primary nucleation peak for Al nanocrystals followed by secondary or tertiary crystallization reactions involving intermetallic phases [34-35]. The signal from the primary nucleation of Al_{fcc} nanocrystals is so weak in the isothermal DSC trace, and there is no obvious peak that could be detected by normal DSC and XRD. Recently, Y. Shen et al. developed a novel method to precisely confirm the onset time of primary crystallization for Al-based MGs based on the Flash DSC [25]. For MGs, the compositional dependences of glass transition temperature before and after primary crystallization are significantly different and there should be divergent evolution paths with the increase of isothermal annealing time. Thus, this method provides an opportunity to separate the

primary crystallization from the relaxation and then confirms the onset time of primary crystallization (delay time for primary crystallization) based on the sensitive nanocalorimetric Flash DSC. Here, for $Al_{90}Sm_8Ag_2$, the heat flow curves with different annealing times for every annealing temperature were measured by Flash DSC (The detailed heat flow curves are seen in the Fig. 7) and the plot of glass transition temperature and annealing time at 150^{o}C is shown in the insertion of Fig. 6(b). Finally, the partial TTT diagram was determined in Fig. 6 (b). For the AlSm-based MG in this work, the temperature range of interest was near the boiling point of water. Therefore, by extrapolating the plot of annealing temperature and annealing time, we can estimate the onset time of primary crystallization near 100^{o}C, about $3.27*10^6$ s (~29 days). These results show that the $Al_{90}Sm_8Ag_2$ MG has a good stability.

Figure 6(c) presents the scheme of a simple imprinting experiment on the surface of $Al_{90}Sm_8Ag_2$ ribbon with large width (about 5mm). A soft rubber cylinder was placed under the MG thin ribbon to provide a soft platform for imprinting. The steel mold used is also shown in the top right part of Fig. 6(c). The bottom right picture of Fig. 6(c) displays the distinct impression of "UW" pattern on the surface of the $Al_{90}Sm_8Ag_2$ ribbon in boiling water at about 100 °C demonstrating the good thermoplastic processability similar to conventional polymeric materials. The final part after imprinting in the boiling water remains fully glassy as confirmed by the XRD results (the detailed results were shown in the Fig. 8), consistent with the TTT diagram (Fig. 6(b)). Recently, thermomechanical data storage was demonstrated by forming nanoindentations through Joule heating of scanned nanotips using a polymer as the storage medium [36]. For this application, there is an advantage in the increased precision and good imprintability for MGs with high elastic modulus [37]. In view of this good imprintability at low temperature for AlSm MGs in this work, it may be useful as a data storage medium.

4.Summary

In summary, we exploited a series of AlSm-based MG systems with low glass transition temperature being close to the boiling point of water, combined with a new method based on the Flash DSC to confirm the glass transition temperature for Al-based MGs. These AlSm-based MG systems display good thermoplastic formability near the boiling point of water. These results indicate the molding, shaping, and imprinting at low temperature for AlSm-based MGs could make the manufacture process as cheaper, convenient, and in large-scale as for thermoplastics.

References

[1] N. March and M. Tosi, Polymers, Liquid Crystals and Low-Dimensional Solids (Plenum, New York, 1984).

[2] W. Fred and J. R. Billmeyer, Textbook of Polymer Science (Wiley, New York, 1984).

[3] I. M. Hodge, Science 267 (1995) 1945-1947.

[4] G Duan, A. Wiest, M. L. Lind, J. Li, Won-Kyu Rhim, W. L. Johnson, Adv. Mater. 19 (2007) 4272-4275.

[5] J. Schroers, Q. Pham, A. Peker, N. Paton, R.V. Curtis, Acta Mater. 57 (2007) 341-344.

[6] J. Schroers, Adv. Mater. 22 (2010) 1566-1597.

[7] J. Schroers, N. Paton, Advanced Materials & Processes, 164 (2006) 61–63.

[8] N. Nishiyama, A. Inoue, Materials Transactions Jim 40 (1999) 64–71.

[9] Y. Saotome, K. Itoh, T. Zhang, A. Inoue, Scr. Mater. 44 (2001) 1541–1545.

[10] Y. Saotome, S. Miwa, T. Zhang, A. Inoue, Journal of Materials Processing Technology 113 (2001) 64–69.

[11] Y. Kawamura, H. Kato, A. Inoue, T. Masumoto, Appl. Phys. Lett. 67 (1995) 2008–2010.

[12] J. Schroers, C. Veazey, M.D. Demetriou, W.L. Johnson, J. Appl. Phys. 96 (2004) 7723–7730.

[13] H. Soejima, N. Nishiyama, H. Takehisa, M. Shimanuki, A. Inoue, J. Metastable and Nanocrystalline Mater. 24 (2005) 531.

[14] A. A. Kundig, T. Schweizer, E. Schafler, J. F. Loffler, Scr. Mater. 56 (2007) 289–292.

[15] B. Zhang, D. Q. Zhao, M. X. Pan, W. H. Wang, A. L. Greer, Phys. Rev. Lett. 94 (2005) 205502.

[16] J. F. Li, D. Q. Zhao, M. L. Zhang, W. H. Wang, Appl. Phys. Lett. 93 (2008) 171907.

[17] K. Zhao, X. X. Xia, H. Y. Bai, D. Q. Zhao, W. H. Wang, Appl. Phys. Lett. 98 (2011) 141913.

[18] H. B. Yu, X. Shen, Z. Wang, L. Gu, W. H. Wang, H. Y. Bai, Phys. Rev. Lett. 108 (2012) 015504.

[19] A. L. Greer, Science 267 (1995) 1947-1953.

[20] A. Inoue, Prog. Mater. Sci. 43 (1998) 365-520.

[21] P. Gargarella, C.S. Kiminami, M.F. de Oliveira, C. Bolfarini, W.J. Botta, J. Alloys Compd. 495 (2010) 334-337.

[22] J. Wang, Y. Liu, S. Imhoff, N. Chen, D. Louzguine-Luzgin, A. Takeuchi, M. Chen, H. Kato, J. Perepezko, A. Inoue, Intermetallics 29 (2012) 35-40.

[23] W. H. Wang, Progress in Materials and Science. 57 (2012) 487-656.

[24] J. H. Perepezko, S. D. Imhoff, J. Alloy. Comp. 504 (2010) 222-225.

[25] Y. Shen, J. H. Perepezko, The Investigation of the Nucleation Delay Time in Al-based Metallic Glasses by the High Rate Calorimetry. To be published.

[26] G. Wilde, H. Sieber, J. H. Perepezko, Scr. Mater. 7 (1999) 779-783.

[27] J. Jackle, Rep. Prog. Phys. 49 (1986) 171-231.

[28] J. E. Mark, *Polymer Data Handbook.* Oxford University Press, Oxford, 1999.

[29] N. Li, X. N Xu, Z. Z. Zheng, L. Liu, Acta Mater. 65 (2014) 400–411.

[30] P.G. Debenedetti, F. H. Stillinger, Nature 410 (2001) 259-267.

[31] W. L. Johnson, MRS Bull. 24 (1999) 42-56.

[32] W. H. Wang, Prog. Mater. Sci. 52 (2007) 540-596.

[33] C. A. Schuh, T. C. Hufnagel, U. Ramamurty, Acta Mater. 12 (2007) 4067-4109.

[34] Wu, R.I.I., *Amorphous phase formation and nanostructure synthesis in aluminum-based alloys*. 2001, The University of Wisconsin - Madison: Ann Arbor.

[35] Y. Shen, J. H. Perepezko, J. Alloy. Compd. 707 (2017) 3-11.

[36] G. Marsh, Mater. Today 6 (2003) 38-43.

[37] W. H. Wang, Progress in Materials Science 57 (2012) 487-656.

Figures and Figure captions

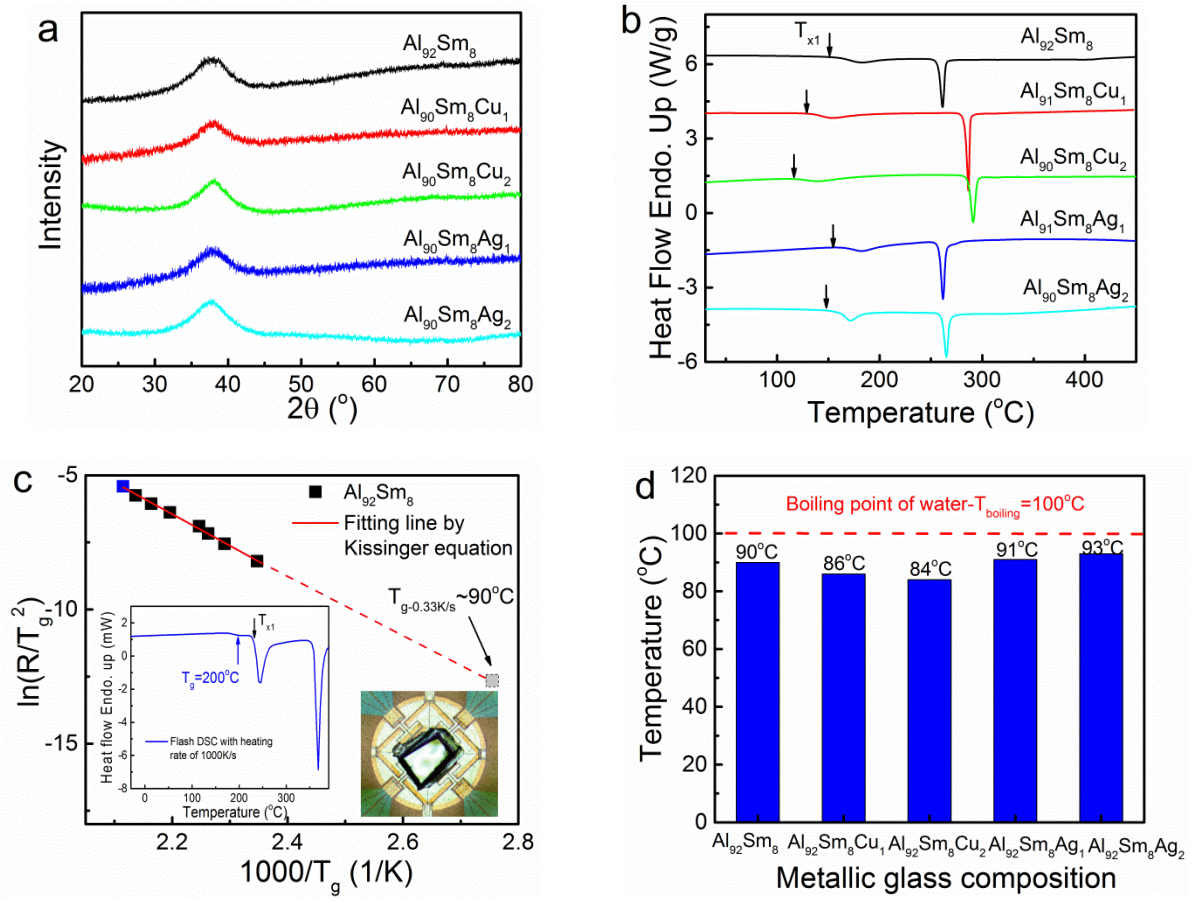

Figure 1. (a) XRD patterns for five AlSm-based MGs. (b) DSC heat flow curves with heating rate of 20K/min for five AlSm-based MGs. (c) Kissinger plot for $Al_{92}Sm_8$ MG by Flash DSC. The inserted plot gives one typical heat flow curve by Flash DSC with heating rate of 1000K/s and the inserted optical image shows the tiny sample loaded on the chip. (d) Histogram of glass transition temperature for AlSm-based MGs. The red dashed horizontal line gives the boiling point of water (100^{o}C).

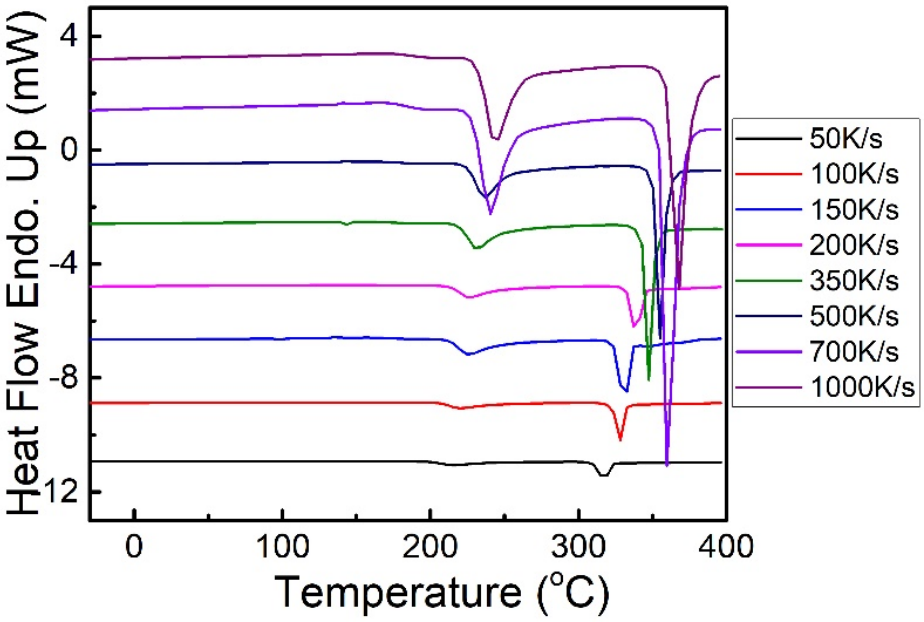

Figure 2. Heat flow curves with different heating rates by Flash DSC for $Al_{92}Sm_8$ MG.

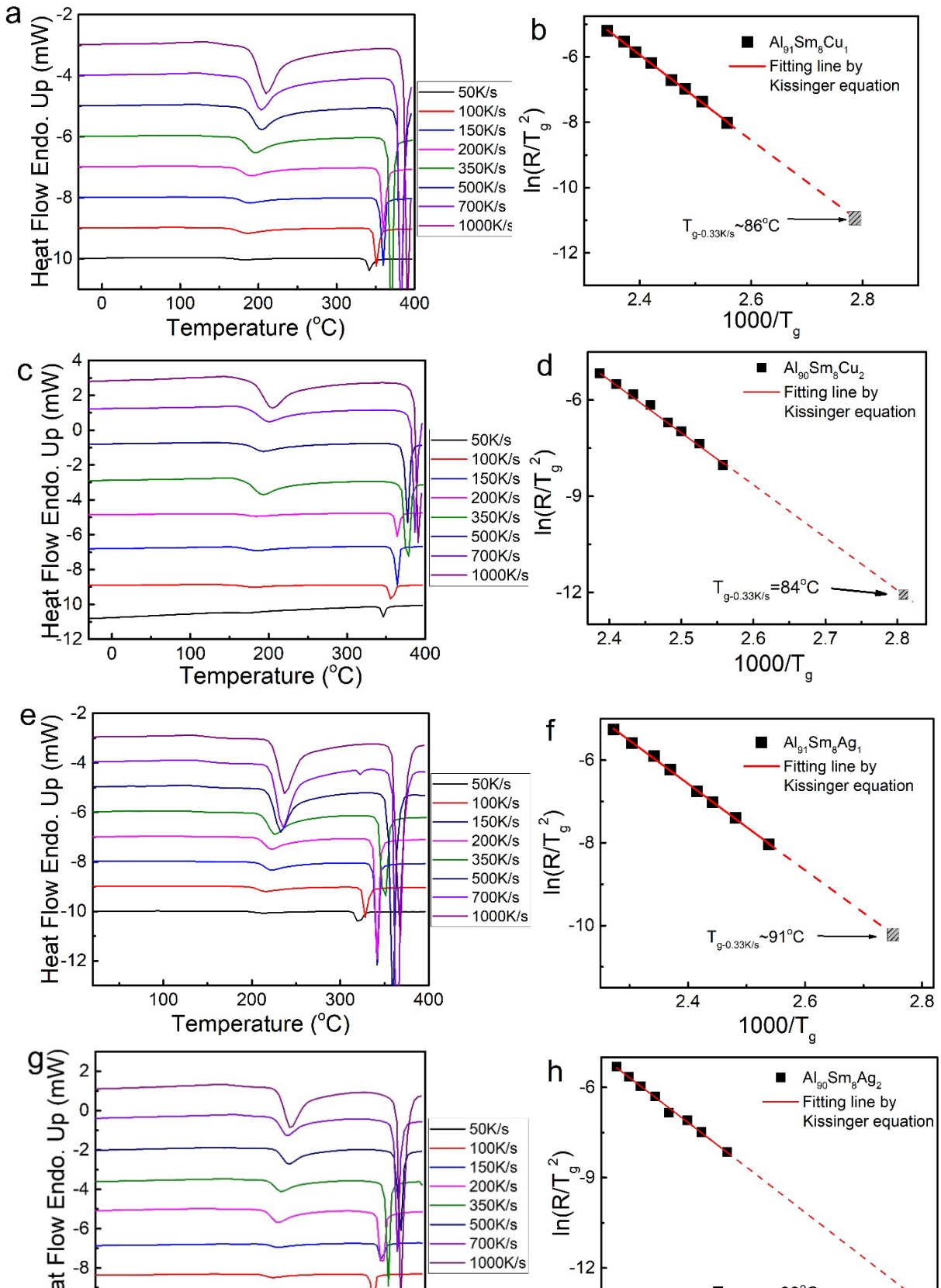
a
Heat Flow Endo. Up (mW)
Temperature (°C)
50K/s
100K/s
150K/s
200K/s
350K/s
500K/s
700K/s
1000K/s
b
Al91Sm8Cu1
Fitting line by
Kissinger equation
Tg-0.33K/s~86°C
ln(R/Tg2)
1000/Tg
c
Heat Flow Endo. Up (mW)
Temperature (°C)
50K/s
100K/s
150K/s
200K/s
350K/s
500K/s
700K/s
1000K/s
d
Al90Sm8Cu2
Fitting line by
Kissinger equation
Tg-0.33K/s=84°C
ln(R/Tg2)
1000/Tg
e
Heat Flow Endo. Up (mW)
Temperature (°C)
50K/s
100K/s
150K/s
200K/s
350K/s
500K/s
700K/s
1000K/s
f
Al91Sm8Ag1
Fitting line by
Kissinger equation
Tg-0.33K/s~91°C
ln(R/Tg2)
1000/Tg
g
50K/s
100K/s
150K/s
200K/s
350K/s
500K/s
700K/s
1000K/s
h
Al90Sm8Ag2
Fitting line by
Kissinger equation
ln(R/Tg2)

Figure 3. Heat flow curves with different heating rates by Flash DSC and the T_g confirmation by extrapolating the Kissinger equation for AlSm-based MG systems. (a)-(b) $Al_{91}Sm_8Cu_1$; (c)-(d) $Al_{90}Sm_8Cu_2$; (e)-(f) $Al_{91}Sm_8Ag_1$; (g)-(h) $Al_{90}Sm_8Ag_2$.

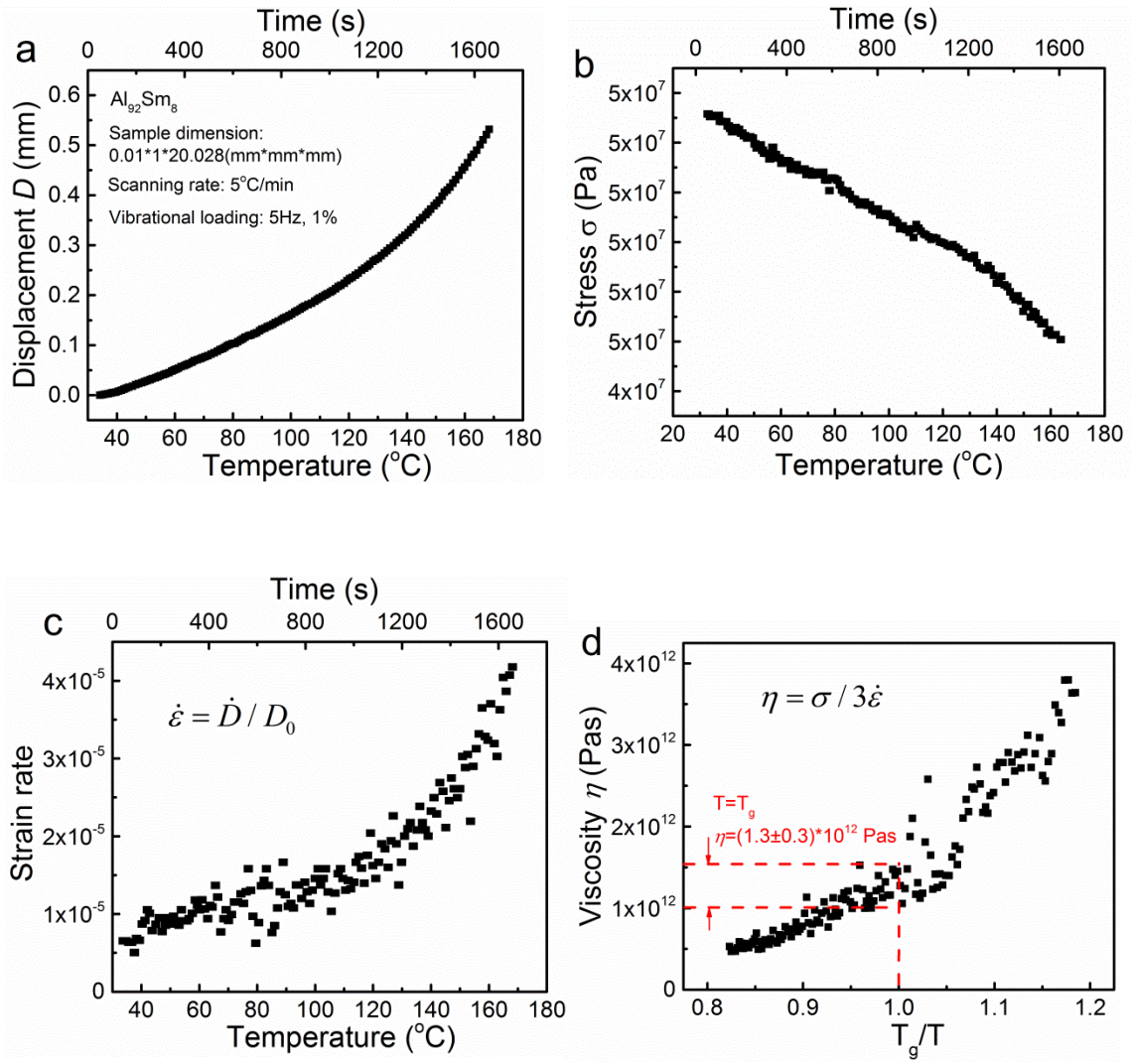

Figure 4. (a) The displacement-temperature (time) curve measured by vibrational load method. (b) The stress-temperature (time) curve measured by vibrational load method. (c) The

corresponding strain rate–temperature (time) curves deduced from the displacement–time curves. (d) The calculated temperature vs. viscosity curve based on the displacement–time curves.

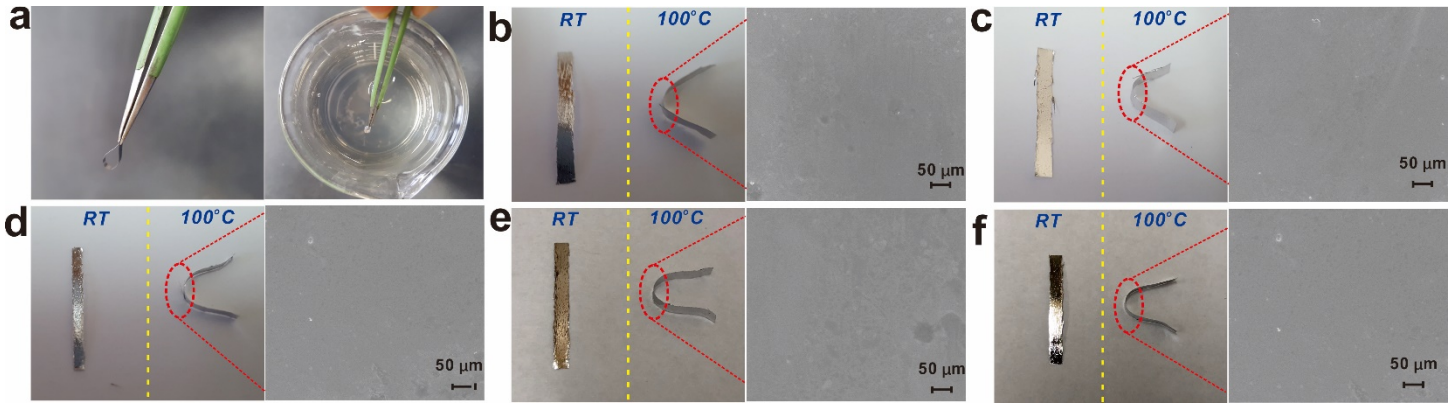

Figure 5. (a) The contrast experiments of thermoplastic deformation at room temperature and in the boiling water. The morphology of two ribbon pieces after releasing for five AlSm-based MG ribbons at room temperature and in the boiling water: (b) $Al_{92}Sm_8$; (c) $Al_{91}Sm_8Cu_1$; (d) $Al_{90}Sm_8Cu_2$; (e) $Al_{91}Sm_8Ag_1$; (f) $Al_{90}Sm_8Ag_2$. The right pictures give the SEM images of the microscopic regions with maximum curvature of the above deformed pieces in the boiling water.

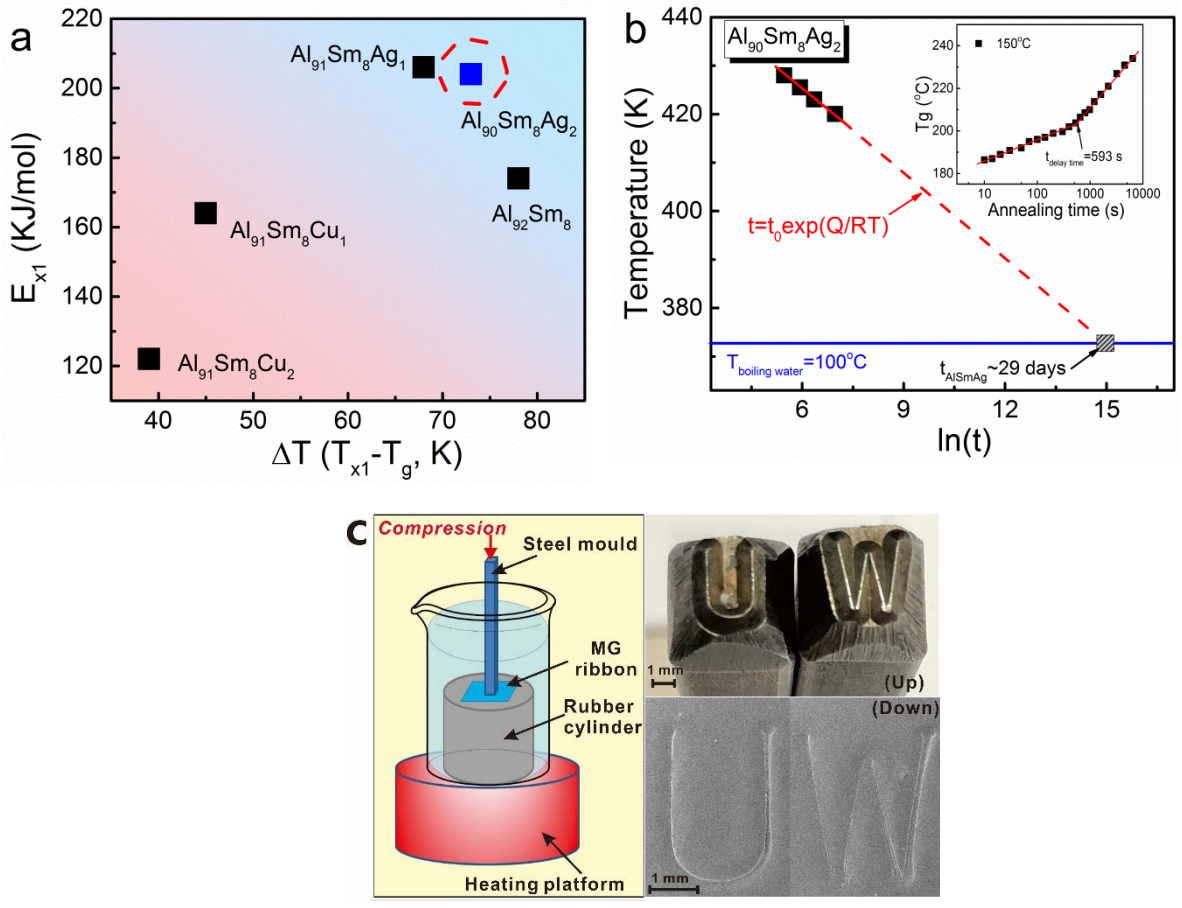

Fig. 6. (a) The plot of ΔT and E_{x1} for five AlSm-based MGs. (b) Time-temperature-transformation (TTT) diagram at low temperature for $Al_{90}Sm_8Ag_2$ MG. (c) The scheme of one simple imprinting experiment (left) and the impression of "UW" pattern on the surface of the $Al_{90}Sm_8Ag_2$ ribbon in boiling water (bottom right). The steel mold used is shown in the top right.

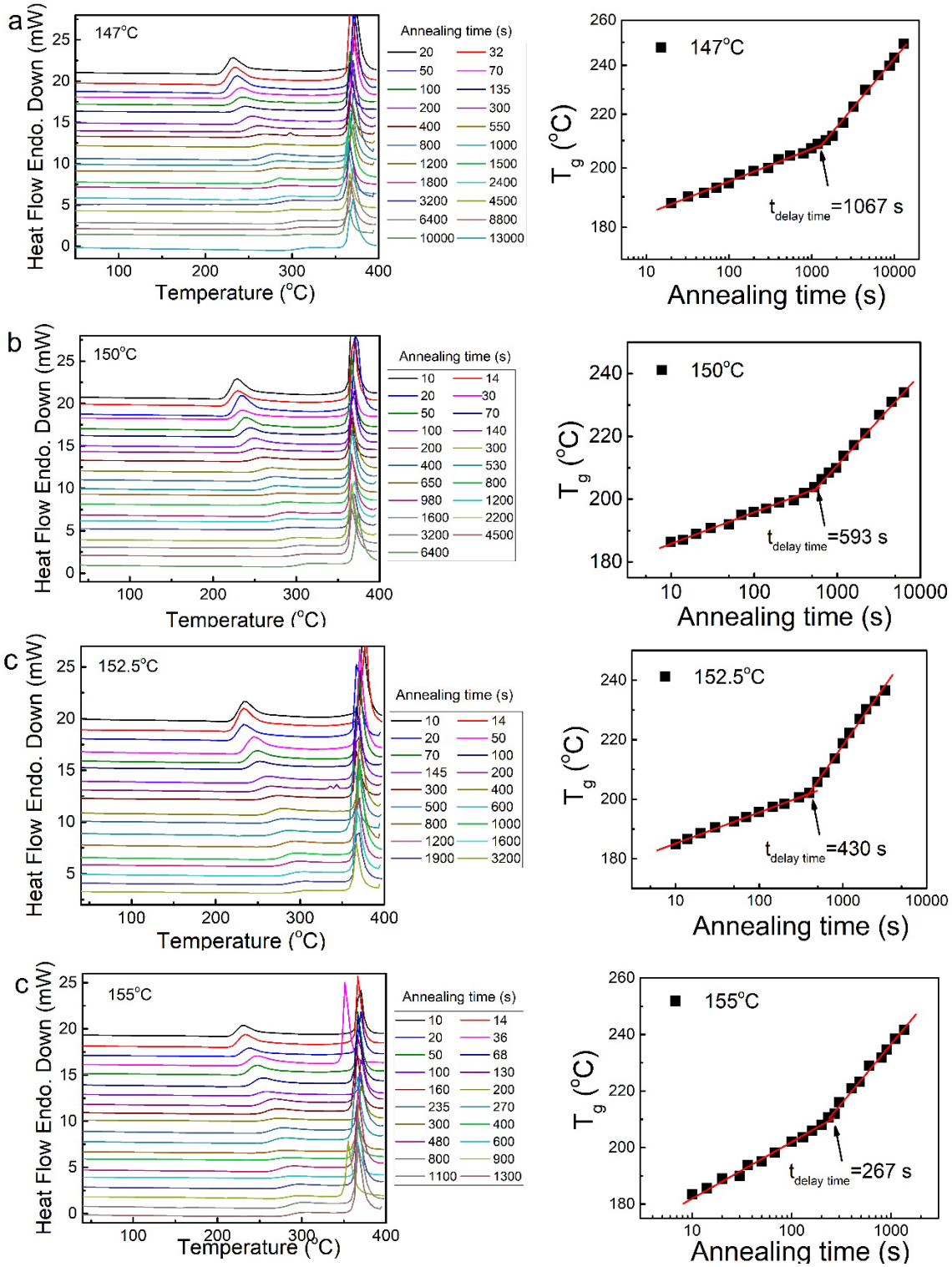

Figure 7. Confirmation of delay time for primary crystallization in $Al_{90}Sm_8Ag_2$ MG: (a) 147°C; (b) 150°C; (c) 152.5°C; (d) 155°C. The left plots are the heat flow curves with different annealing time for one annealing temperature by Flash DSC and the right plots give the glass transition temperature evolution with the annealing time.

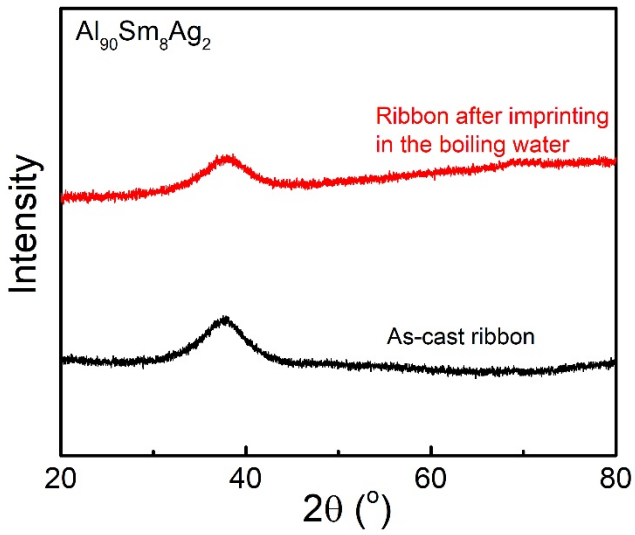

Figure 8. XRD comparison between as-cast ribbon and the ribbon after imprinting in the boiling water for $Al_{90}Sm_8Ag_2$.

Table 1. Glass transition temperature T_g, primary crystallization temperature T_{x1}, secondary crystallization temperature T_{x2}, the supercooled liquid region $\Delta T=T_{x1}-T_g$, primary crystallization activation energy E_{x1}.

Composition	T_g (°C)	T_{x1} (°C)	T_{x2} (°C)	ΔT (T_{x1}-T_g) (°C)	E_{x1} (KJ/mol)
$Al_{92}Sm_8$	90	168	257	78	174
$Al_{91}Sm_8Cu_1$	86	131	283	45	164
$Al_{90}Sm_8Cu_2$	84	123	288	39	122

$Al_{91}Sm_8Ag_1$	91	164	259	73	204
$Al_{90}Sm_8Ag_2$	93	161	262	68	206

Part III

The thermal stability and novel nucleation dynamics of Zn-based metallic glass via ultrafast Flash DSC

1. Introduction

Metallic glasses (MGs) have been investigated extensively during the past decades in consideration of their outstanding mechanical and chemical properties.[1-2] Compared to the crystalline metals and alloys, MGs exhibit ultrahigh specific strength, large elastic strain limit, high fracture toughness, good corrosion resistance and excellent soft magnetic properties arising from the unique atomic structure without long-range periodic packing order and variable chemical composition.[3-4] Moreover, some MGs show good thermoforming deformation ability like plastics in the supercooled liquid due to viscous flow workability and isotropy which qualifies them as a candidate in the production of small-scale micro-electro-mechanical devices by molding, embossing and imprinting.[5-8] Recently, a series of novel MGs have been developed with exceptionally low glass transition temperature (around 100-200^{o}C), high glass-forming ability and large supercooled liquid region.[5, 9-12] These MGs include Ce-, CaLi-, Sr-, Zn-, and Au-based MGs exhibit the temperature driven plastic-like homogenous deformation behaviors without shear bands at low temperature range and are thus named as metallic plastics (MPs). On the other hand, these MPs are metastable in their supercooled liquid region in contrast to traditional thermoplastics, which largely impedes the potential applications of MPs. Meanwhile, by selectively tuning the morphology and number density of secondary crystalline phases in supercooled liquid region, the MG composites with large compression and tensile plasticity have been successfully developed.[13-15] However, in order to advance the thermoplastic-forming processes and other practical applications for MGs, more knowledge about nucleation and crystallization kinetics in the supercooled liquid state and glass state is essential.

Recently, there have been several studies focusing on the structural and dynamic heterogeneity of MGs based on the various advanced detecting methods.[16-21] The results indicate that the MGs are not homogeneous at the nanoscale and there exist spatial heterogeneities or flow defects (also termed as liquid-like zones, flow units or weakly bonded regions). [16-21] For example, Ichitsubo et al. revealed the microstructure of one partially crystallized Pd-based MGs by utilizing the ultrasonic annealing method and directly inferred a plausible microstructural model of fragile MGs composed of strongly bonded regions surrounded by weakly bonded regions.[20] Compared to the homogenous elastic glass matrix, these nanoscale heterogeneities show viscoelastic properties, such as low modulus, low viscosity and high atomic mobility. Thus, MGs can be simply considered as a random distribution of viscoelastic defects in the elastic matrix.[21] The intrinsic heterogeneous

structure in MGs was indicated to determine the nucleation and crystallization behaviors, which is of great importance for fundamental research and practical applications.[20] However, unfortunately, the rapid crystallization nucleation and growth of MGs limit most experimental kinetics studies in the supercooled liquid region to exclude the examination of the relationship between the nucleation and the intrinsic heterogeneous structure for MGs.

For conventional thermo-analytical methods such as differential scanning calorimetry (DSC) or differential thermal analysis (DTA), it is not possible to achieve constant heating and cooling rates higher than a few K/s, so that in-situ probing of the competition between glass formation and crystal nucleation from an equilibrium liquid and the following crystallization process is limited to systems with sluggish kinetics. However, a recently developed chip-based fast differential scanning calorimeter enables thermo-analytical measurements at orders of magnitude higher rates. A commercial fast differential scanning calorimeter instrument (Mettler Toledo Flash DSC 1)[22-23] can reach the maximum heating and cooling rate of several 10^4 K/s and 10^3 K/s. This advanced thermo-analytical equipment has generally been applied to study the nucleation and crystallization behaviors of all kinds of materials, such as polymers,[24] organic materials[25] and phase-change materials[26]. In addition, there are several studies focusing on the MGs, especially for some MGs systems with sluggish thermodynamic behaviors, such as the Au-based MGs.[27-32] The powerful capability of heating and cooling so fast enables the researchers to investigate the abnormal phase transition and extreme kinetic behaviors, such as the polyamorphism and fast nucleation and crystallization in amorphous materials. Therefore, such an emerging calorimetric technique with ultrafast heating and cooling rate will provide a good opportunity to exploit new amorphous materials and study some new physical properties and behaviors of existing amorphous materials, such as the rapid crystallization nucleation and growth in marginal MGs.

In this study, we selected the Zn-based MG system considering the low glass transition temperature, low elastic modulus and good superplastic forming ability. By deploying a Zn-based MG with low glass transition temperature and Flash DSC with ultrafast cooling and heating rate, a complete characterization was carried out for the thermodynamic and nucleation kinetics behaviors in a Zn-based MG. This method has allowed for the determination of the critical cooling rate and heating rate, various thermodynamic properties, the kinetic fragility property and the temperature-time-transformation (TTT) diagram within the supercooled liquid temperature zone. To study the effect of intrinsic structural heterogeneities of MGs on the nucleation and the following crystallization behaviors in the supercooled liquid zone, we applied a new measurement method by fast heating the glass sample into the target temperature rather than cooling from liquid. The measured TTT curve displays a unique double-nose shape so that there exist two separate crystallization paths in the overall transformation reaction. Meanwhile, the TTT curves by directly undercooling from liquid were also obtained to compare the difference of nucleation kinetic behaviors by two different methods. Moreover, the cooling rate and the structural relaxation influences on the double nosed TTT curves were studied. Finally, a heterogeneous nucleation model is proposed to further investigate the properties of two nucleation sites including the potential nucleation site density and the contact angle between the nucleus and the glass matrix. This model provides a good fit of the experimental TTT diagram by heating from glass and the cooling rate and structural relaxation effect on two potential nucleation sites are well evaluated based on the heterogeneous nucleation model and the measured experimental results.

2. Experimental details

The ingot with nominal composition of $Zn_{40}Mg_{11}Ca_{31}Yb_{18}$ was prepared by induction melting from commercial pure metallic elements and was melted for three times to confirm the homogeneity. Metallic glasses (MGs) ribbons with the same thickness of about 25 μm (2-3 mm wide) were prepared by melt-spinning method using a Cu wheel at a tangential velocity of ~55 m/s in an inert argon atmosphere. The amorphous nature of the as-spun ribbon alloy was ascertained by X-ray diffraction (Bruker D8 Discover Diffraction with Cu K_α radiation), and differential scanning calorimetry (PerkinElmer DSC Diamond).

A PerkinElmer Diamond DSC instrument was used to characterize the thermodynamic and kinetic properties with heating rate 20 K/min. A high-rate differential scanning calorimeter with chip sensors (Flash DSC 1, Mettler Toledo) was used for both isothermal heat treatment and in-situ thermal analysis. The ribbon samples were cut into small pieces of approximately 0.16mm×0.16mm to be loaded into the Flash DSC chip. The temperature range for Flash DSC chips is from -90 ^oC to 450 ^oC. To prevent the oxidation of the samples during heating, a flow of N_2 gas (15 ml/min) was applied during the whole measurement. The allowable mass of the tiny sample pieces for Flash DSC measurement is between 10 ng and 1 mg. To further characterize the microstructure of onset crystalline Flash DSC samples, we applied Plasma Focused Ion Beam (FIB) milling system to prepare the Transmission Electron Microscope (TEM) specimen (Tecnai 12 TEM).

3. Results

3.1. Thermodynamic parameters characterization and the determination of critical cooling rate for glass formation

The amorphous nature of Zn-based ribbon sample was confirmed by X-ray diffraction in Fig. 1(a), and differential scanning calorimetry in Fig. 1(b). The values of thermodynamic parameters including the glass transition temperature, the crystallization temperature, the melting temperature and the liquidus temperature were obtained from Fig. 1(b) and are listed in Table I. A typical heat flow curve by Flash DSC scanning at a heating rate of 1000 K/s for the Zn-based MG ribbon is shown in Fig. 2(a). The inserted picture in Fig. 2(a) illustrates the optical image of a tiny sample on the sample cell of Flash DSC chip. With the increase of temperature, an obvious glass transition can be observed followed by an exothermic crystallization peak and the melting of the MG sample. Then the MG sample was amorphized in situ by quenching an equilibrium liquid from 703 K (higher than the liquidus temperature, 666 K) to room temperature with a cooling rate of 2100 K/s prior to the following measurement to reveal the glass transition during heating that also appears in Fig. 2a. Therefore, the following heat flow curves provide the measurements of the glass transition temperature upon heating ($T_{g,h}$), the crystallization onset temperature (T_x), the crystallization enthalpy (H_x), the melting onset temperature (T_m), the melting enthalpy upon heating (H_m), and the onset glass transition temperature ($T_{g,c}$) upon cooling.

To determine the critical cooling rate range (R_c) for glass formation in Zn-based MG, various cooling various cooling rates from 750K/s to 3000K/s were applied and the crystallization enthalpy (H_x) on subsequent heating with the same heating rate of 1000K/s was measured. Due to the tiny sample, the mass of Flash DSC sample cannot be directly measured precisely. Thus, for an effective comparison, a single sample was used during the above heating and cooling tests. Fig. 2(b) gives the applied temperature–time program. The sample was first heated fast (1000 K/s) to the destination temperature (T_{end}=430^oC, higher than T_L=393^oC), cooled from the melt at different

cooling rates from 750 K/s to 3750 K/s and then heated again at 1000 K/s up to T_{end}. From Fig. 2(c) and 2(d), the enthalpy of the same sample increases, and the melting temperature does not change with the increase of cooling rate. For the sample cooled at a high enough cooling rate, the H_x becomes a constant, which implies the sample is totally amorphous. The measured values of H_x corresponding different cooling rates are listed in the Table 2 and are plotted in Fig. 2(d). One can clearly see that the critical cooling rate range R_c for glass formation is determined to be in the range of 1900-2000 K/s.

3.2. Fragility and the critical heating rate for preventing crystallization during heating

When a glass forming liquid is supercooled through the glass transition region, the viscosity of system has a huge increase of about twelve orders in magnitude.[33] For different liquids, the rheologic behaviors with temperature approaching the glass transition temperature follow different patterns. These rheologic patterns during slowing-down process can be well characterized by one parameter named "fragility", proposed by Angell,[33] to describe different scaling behaviors of supercooled liquids with respect to temperature: $m = \left.\frac{d\log\eta}{d(T_g/T)}\right|_{T=T_g}$, where m is the fragility parameter and η is the liquid viscosity. For fragile liquids with a high m value the viscosity displays a strongly non-Arrhenius style; in contrast strong liquids display an Arrhenius-like dependence with temperature. The relaxation times τ of supercooled liquids evolving with temperature T can be approximately characterized by the Vogel-Tammann-Fulcher (VTF) equation,

$$\tau = \tau_0 \exp(\frac{D^* T_0}{T - T_0}) \quad (1)$$

where τ_0 is the infinite temperature relaxation time, D^* and T_0 are fitting parameters (Viscosity can also be described by similar VFT equation).[34-35] D^* is commonly called as the VFT strength parameter and T_0 is the theoretical Kauzmann temperature interpreted as the extrapolation of the glass transition temperature to infinitesimally slow cooling rates. When the different heating rates are applied to heat a glassy sample with the same cooling rate, both the glass transition signal and crystalline peak shift to higher temperatures, as shown in Fig. 3(b) and Fig. 3(c). Considering that the width of the total glass transition process, $\Delta T_g = T_{g\text{-}end} - T_{g\text{-}onset}$, increases with the increase of heating rate in Fig. 3(b) and Fig. 3(c), the relaxation time for the glass transition at each heating rate R can be roughly calculated as $\tau_g = (T_{g\text{-}end} - T_{g\text{-}onset})/R$.[36] Thus, based on the relationship between the glass transition temperature T_g and the corresponding relaxation time τ_g confirmed by Eq. (1), the values of the fitting parameters are obtained in the insertion of Fig. 3(d). After determining the value of the parameters, the fragility parameter m can be determined using the equation:[35]

$$m = \frac{D^* T_0 T_g}{(T_g - T_0)^2 \ln(10)} \quad (2)$$

where T_g is the glass transition temperature upon heating with the heating rate of 20K/min. By this method, the fragility parameter for Zn-based MG was determined to be 46. This value indicates the Zn-based MG former displays the strong liquid behavior, which is consistent with other reported results.[12, 37] Especially, from Fig. 3(c), when the heating rate increases into about

15000K/s, the crystalline peak vanishes, and this heating rate of 15000K/s is the critical heating rate R_h to prevent the glassy sample from crystallizing upon heating.

3.3. Crystallization kinetics characterization-Temperature-Time-Transformation (TTT) diagrams by heating from glass and cooling from liquid

The crystallization behavior of MGs can be studied in-situ via Flash DSC by performing isothermal measurements to record the temperature-time-transformation (TTT) diagram for different thermal histories. For the determination of TTT diagrams, there are two different methods : cooling from liquid and heating from glass.[38-41] The method of undercooling from liquid has been widely used to study the glass formation and the nucleation and crystallization by cooling from the liquid.[38-41] In contrast, the second method by heating from as-cast glass is mainly used to study the effect of intrinsic structural heterogeneities of MGs on the nucleation and the following crystallization behaviors in the supercooled liquid zone.[11, 32] Due to the high requirement of ultrafast heating rate to prevent the crystallization during heating, this method is rarely applied. Recently, with the development of the ultrafast Flash DSC instrument (the maximum heating rate can reach $4*10^4$ K/s) this method provides a good opportunity to study the correlation between the intrinsic glass structure and the nucleation and crystallization during heating. Thus, in this part, we firstly applied this novel method by fast heating from glass to measure the TTT diagram. Then the corresponding TTT diagram by fast cooling from liquid was also obtained to compare the difference of nucleation and crystallization for these two methods. The temperature programs applied (method (1) by fast heating from glass and holding, and method (2) by fast cooling from liquid and holding) are shown in Fig. 4(a). First, according to method (1), the sample was heated into 703K at 100 K/s, which is higher than the liquidus temperature (666K), for 4s to confirm completely melting (From Fig. 9, the time of the whole melting from onset to end is 0.5s). The melt was then quenched to 298 K at a cooling rate of $1*10^4$ K/s (named glass I) to achieve a fully amorphous state and subsequently heated at a rate of $2*10^4$ K/s to the temperature of the isothermal measurement. Since the melting temperature (354^{o}C) is much lower than the maximum temperature of the Flash DSC (450^{o}C), the complete TTT diagram could be obtained from the glass transition temperature to the melting temperature. The isothermal experimental results that reveal a low temperature part and a high temperature part are shown in Fig. 4(b) and 4(c). It is evident that the onset time for crystallization varies with isothermal temperature. Hence, the complete TTT diagram for Zn-based MG by fast heating from glass can be obtained and is plotted in Fig. 4(d). Interestingly, different from the previous typical C-shaped TTT diagram with only one nose by cooling from liquid,[27, 38-41] the TTT diagram for the Zn-based MG by fast heating from glass in this work displays two noses and a second transformation path (B part marked by orange curve in Fig. 4(d)) separates from the high temperature transformation route (A part marked by green curve in Fig. 4(d)) between 480K and 560K. It should be noted that the typical method[27, 38-41] to obtain the TTT diagram is to undercool the melt and then hold the temperature isothermally and this method is mainly used to characterize the dynamic properties of undercooled liquid. In contrast, the method we applied in this work is to fast heat the glass sample and then hold the temperature isothermally. Due to the ultrafast heating rate for advanced Flash DSC, the intrinsic structure and physical properties of glass sample will not have enough time to relax during heating. Therefore, this novel behavior indicates that the nucleation and crystallization may not simply be described by one transformation mode, and the intrinsic structural heterogeneity for glass state inherited from the liquid[16-21] and complex dynamic properties could play a critical role in the structural relaxation and the following crystallization in the supercooled liquid zone.

Moreover, based on the above TTT curve, the critical cooling rate R_c for glass formation can be estimated to be R_{cB}=6900 K/s by taking isothermal annealing temperatures to the equation $R_c = \frac{T_L - T_n}{t_n}$,[40] where t_n is the nose time, T_L the liquidus temperature, and T_n the nose temperature determined from the TTT diagram. The critical cooling rate range measured by Flash DSC is about 1900-2000K/s, which is much lower than the value of R_{cB}. In view of the non-linearity of nucleation event and the existence of an induction time (or delay time) for nucleation at one temperature, the values of R_{cB} based on the nose method from the experimental TTT curves are always much larger than those determined from constant cooling rate conditions since this method actually relates to the continuous cooling transformation (CCT) diagram.[41]

For the separate transformation paths as shown in the TTT curve by heating from glass I, there are three possibilities: one is that the second transformation path arises from the kinetic superiority of different crystal phases within a narrow temperature range (480-560 K). It is further supposed that these phases are in competition throughout the whole supercooled liquid region, but that the one characterized by the orange curve is suddenly afforded superior kinetics within its temperature range. To test this hypothesis, four isothermal temperatures within and out of this narrow temperature range were specially selected: 330ºC, 250ºC, 230ºC and 190ºC, and the data points corresponding these four temperatures were marked by red stars in Fig. 4(d). From Fig. 5(a), it is evident that only one crystalline peak appears and both the orange and green transformations yield the same crystalline phases. As an additional test, the samples were held at temperatures within the temperature range above and then, once the phase had transformed, the samples were rapidly heated to see if they melt at a temperature different from that for the phase marked by the green transformation curve. From Fig. 5(b), the melting temperatures were the same for the products of both the red and blue transformation curves in the inserted graph of Fig. 5(b). Therefore, the separate transformation paths are not induced by another metastable phase. Meanwhile, XRD measurements were made to further confirm the identity of the crystalline phases formed within different temperature ranges corresponding to the path A and path B (The detailed measurement method for tiny Flash DSC samples is shown in the Fig. 10). For the Flash DSC samples at 330ºC, 250ºC and 190ºC in Fig. 5(c), the results clearly show that the XRD pattern represents the same crystalline phases for all three annealing temperatures, which further indicates that different phases are not involved in the crystallization. The second possibility for the two transformation paths is that the high temperature path is controlled by heterogeneous nucleation and the low temperature path represents homogeneous nucleation. These conditions have been reported for the crystallization reactions in some polymer systems.[42-43] However, for the Zn based BMG the relative undercooling for the low temperature path, $\Delta T/T_m$ is only 0.16 which is too small for the onset of homogeneous nucleation in metallic systems. The third possibility for the separated transformation paths is that the heterogeneous nucleation sites originated from the heterogeneous structure of MGs or other sources are active. It is plausible that the two transformation paths occur in the presence of different heterogeneities. If this were the case, then the relative frequency with which one mode of transformation occurred with respect to the other would be both inversely proportional to the ratio of the surface energies associated with the material and the heterogeneity and directly proportional to the heterogeneity concentration.[44] In this case, if the transformation path A were caused by heterogeneity A and the transformation path B by heterogeneity B, then at both higher and lower temperature, heterogeneity A has a greater concentration, but in a narrow

temperature range (between 480K and 560K), heterogeneity B has a much higher concentration in the material. From this perspective, upon heating the glass sample from low temperature, the potential nuclei are expected to form already near the glass transition considering the deep undercooling, and thus the crystallization peak mainly corresponds to the nuclei growth. Hence, the crystallization process in general is limited by growth at the low-temperature range.[11] The crystallization on heating remains growth-controlled with increasing atomic mobility, but the growth kinetics slows down due to the decreasing of crystallization driving force near the temperature of melting. Based on the above discussions about the possibilities of double-nosed nucleation behaviors, the potential nuclei formed in the glass preparation process of cooling down directly control the following nucleation paths during heating. Thus, the two different potential nucleation sites from the heterogeneous structure of glass lead to the double-nosed TTT diagram. The similar results were also found, but were not analyzed in the Au-based MG.[11, 32]

To further investigate the difference of nucleation behaviors by heating from glass and cooling from liquid, the TTT diagram by cooling from liquid with the cooling rate of 10000 K/s for Zn-based MG was also measured, as is shown in Fig. 6(b). Here, the cooling rate for the cooling method (2) from liquid is the same with that of preparing the glass I for the heating method (1) in order to exclude the effect of the cooling rate (the temperature program of method (2) is shown in Fig. 4(a)). It is obvious to find that the TTT diagram by cooling from liquid appears only one nose compared to the double noses by heating from glass, which is consistent with the previous research.[27, 38-41] The single nosed TTT diagram by method (2) has been observed by many researchers and it has been verified as the result of the competition between the nucleation driving force from undercooling and the diffusion process dependent on the temperature.[31, 38-40] By comparing two TTT diagrams by employing two different methods in Fig. 4(d) and 6(b), one can clearly see that two curves merge at the low-temperature branches, but diverge at high temperatures. For the TTT diagram by cooling from liquid, based on the classical nucleation theory, the nucleation process becomes rate-limiting for crystallization at high temperatures considering that the nuclei have to form at low undercooling with a low driving force.[38-39] At low temperature range, the crystallization is also limited by the growth and the potential nucleation sites come from the formed clusters during the cooling down process. It is the same origin with the crystallization by heating from glass, which makes two TTT curves emerge together. On the other hand, the nucleation and crystallization events above the nose point of the TTT-diagram occurs upon cooling at much longer time scales than upon heating, which leads to a divergence in behavior in the high temperature range.

3.4 Cooling rate effect on the TTT diagrams by heating from glass and cooling from liquid

Based on the quenched-in cluster model of nucleation and crystallization for MGs,[44-46] during cooling down from liquid, the larger the cooling rate, the less time for the cluster formation and thus a reduced number density of retained clusters. Hence, different cooling rates usually induce the distinct microscopic atomic structure and the structural heterogeneities.[47-49] Meanwhile, these formed clusters are actually the potential nuclei during the following nucleation and crystallization.[44-46] Therefore, the cooling rate should play a key role in the nucleation and crystallization behaviors for MGs. To investigate the cooling rate effect on the TTT diagrams by heating from glass and cooling from liquid, a significantly different cooling rate of $3*10^3$ K/s being close to the critical cooling rate for Zn-based MG formation was chosen. The corresponding TTT diagrams by heating from glass and cooling from liquid under the cooling rate of $3*10^3$ K/s (the

formed glass sample was named glass II) were obtained and were shown in the Fig. 6(a) and 6(b), respectively. Obviously, for two kind of TTT diagrams, compared to the TTT diagrams with the cooling rate of $1*10^4$ K/s, both the TTT diagrams with the cooling rate of $3*10^3$ K/s shift to the shorter time range, which indicates that the lower cooling rate accelerates the appearance of the nucleation and crystallization during heating from glass and cooling from liquid.

First, for the TTT curves by cooling from the liquid, there have been many studies.[30-39, 50-51] According to the previous research,[30-39, 50-51] the TTT diagrams by undercooling from liquid can be well fitted and the fitting equations are inserted in the Fig. 6(b) as illustrated by the blue and green curves. The detailed formula derivation and the calculations can be seen. It should be noted that the parameter of Γ includes the information of the potential site density ρ_s. Thus, we can roughly estimate the ratio of the formed nucleation site density for two cooling processes with different cooling rates by comparing the values of Γ. From Table 3, the values of parameter Γ corresponding to the cooling rates of $3*10^3$ K/s and $1*10^4$ K/s are -4.08 and -3.59, respectively. Then, $\Gamma_{3000}-\Gamma_{10000}=\ln(3\pi a^3\eta_0/\rho_s Vk)_{3000}-\ln(3\pi a^3\eta_0/\rho_s Vk)_{10000}=\ln(\rho_{s\text{-}10000}/\rho_{s\text{-}3000})=-0.49$. Thus, $\rho_{s\text{-}3000}/\rho_{s\text{-}10000}=1.63$, which indicates that the nucleation site density for cooling process with cooling rate of $3*10^3$ K/s is larger than that of cooling process with cooling rate of $1*10^4$ K/s. From the perspective of the quenched-in cluster model of nucleation and crystallization,[41, 44-46] the above results about the TTT diagrams by cooling from liquid are reasonable. During cooling down from liquid, the liquid with cooling rate of $3*10^3$ K/s has more time to form the clusters than that for the liquid with cooling rate of $1*10^4$ K/s. Hence, at the same temperature, the formed cluster density for the liquid with cooling rate of $3*10^3$ K/s is larger than that of the liquid with cooling rate of $1*10^4$ K/s. The liquid with cooling rate of $3*10^3$ K/s needs less time to nucleate and generate the first crystallization event, which leads to the shifting to the shorter time range in the TTT diagram for the liquid with cooling rate of $3*10^3$ K/s.

Second, for the TTT curves by heating from glasses, the potential nucleation sites (the formed clusters during the cooling down) for glass II (cooling rate is $3*10^3$ K/s) should be larger than that of glass I (cooling rate is $1*10^4$ K/s). Thus, the nucleation time for glass II should be shorter than that of glass I. From the TTT diagrams in Fig. 6(a), both of noses for TTT diagram with cooling rate of $3*10^3$ K/s shift into the shorter time range, which is consistent with the previous discussions and further confirm that the nucleation site density for two different potential nucleation sites increase with the decrease of cooling rate. Moreover, it is interesting to find that the nose temperature changes for the two nucleation sites display different paths in Fig. 6(a): for site A, the temperature of the nose increases from 310 ^{o}C to 314 ^{o}C and the increase of temperature is about 4 ^{o}C; in contrast, the temperature of the nose for the site B increases from 255 ^{o}C to 275 ^{o}C and there is almost 20 ^{o}C increase. In addition, it appears that the two nucleation paths seem to gradually approach each other with the decrease of cooling rate. The two nucleation paths may merge together when the cooling rate increases above a critical value. On the other hand, due to the similarity of the lower cooling rate and structural relaxation,[52-54] the microscopic heterogeneous structure evolution originated from structural relaxation[52] can induce a more obvious change for the TTT diagram by heating from glass. Thus, the annealing treatment should play the same role with the lower cooling rate in the tuning the nucleation path evolution.

3.5 Structural relaxation effect on the TTT diagrams by heating from glass I

The temperature program for the annealing treatment was inserted in the Fig. 6(a). The annealing temperature was chosen as 353 K (0.9 T_g) and the annealing time is 2 hours (7200 s). The obtained TTT diagram by heating from the annealed sample is shown in the Fig. 6(a). It is surprising to find that there only appears one nose for annealed glass sample compared to the double nosed TTT diagrams for as-cast glass samples. The red arrows gives the evolution of the nose points and they obviously exhibit the evolution of nucleation path from two paths to single path with the decrease of cooling rate and structural relaxation. From the previous research about the structural relaxation effect on the microscopic structure and the heterogeneity in MGs,[52-53, 55-56] structural relaxation brings about the change of the microscopic structure and the heterogeneity compared to the as-cast counterparts. The spatial heterogeneities or flow defects[16-21] in MGs gradually tend to decay with the decrease of the cooling rate or the increase of the structural relaxation, which happens to correspond to the merging of the two different nucleation paths in Fig. 6(a). what is more, from Fig. 6(a), the site B displays a more evident and larger change with the decrease of cooling rate or under the deeply structural relaxation. Hence, it may reveal that the novel nucleation path of B site originates from these spatial heterogeneities or flow defects in MGs. The previous research about the ultrasound-accelerated crystallization in Pd-based MG[20] reported the similar results and the different local regions with different bonding display the different nucleation and crystallization paths.

For the previous nucleation model for analyzing the TTT diagram by cooling from liquid based on the Stokes–Einstein equation,[30-39, 50-51] it should be noted that there is evidence that the equation of Stokes-Einstein does not hold for temperatures around T_g, but starts to fail around 1.2–1.3 T_g.[50, 57] Hence, the previous model is not applicable to study the nucleation behaviors exhibited by the TTT diagram by heating glasses. Meanwhile, considering that the intrinsic heterogeneous structure of MGs determines the following nucleation and crystallization, a new nucleation model is necessary. In the discussion section, we propose a new heterogeneous nucleation model based on multiple heterogeneous nucleation sites to investigate the unique nucleation and crystallization behaviors by heating from glass and the cooling rate and structural relaxation effects in Zn-based MG.

4. Discussions

4.1 A heterogeneous nucleation model based on two nucleation sites

The unique crystallization kinetics of the Zn-based MG can be analyzed in terms of classical nucleation theory and the incorporation of two different heterogeneous sites. According to the classical nucleation theory for the heterogeneous nucleation, the steady state nucleation rate J can be expressed as,[48]

$$J = \rho_s Z \beta \exp[-\frac{\Delta G^* f(\theta)}{kT}] \quad (3)$$

where ρ_s is the nucleant density, Z is the Zeldovich factor, β is the atom attachment frequency to the evolving nucleus, ΔG^* is the nucleation barrier, $f(\theta)$ represents the catalytic potency of the nucleation site with a range $0 < f(\theta) < 1$ and k is Boltzmann's constant. For spherical-cap nuclei $f(\theta)=(2-3\cos\theta+\cos^3\theta)/4$, where θ is the contact angle between the nucleus and the catalytic substrate. Here, for the sake of simplicity, we assume the nucleus is spherical-shaped. Thus, the

nucleation activation barrier of a spherical nucleus, ΔG^*, can be obtained from classical nucleation theory as:[58] $\Delta G^*=(16\pi/3)(\sigma^3/\Delta G^2_v)$, where σ is the interfacial energy between liquid and solid, $\Delta G_v=\Delta H(T_m-T)/T_m$ is the driving force for crystallization,[58-59] where ΔH is melting enthalpy, and T_m is melting temperature. The method to determine the appropriate value for ΔG_v depends on the crystallization reaction model competing with glass formation during cooling. In this case, a eutectic mode is considered since it is not clear which of the observed crystallization products nucleated first. However, the difference in the subsequent analysis results based upon using either the measured T_m or T_L values is minor and does not affect the conclusions. For atom attachment frequency β, there are two perspectives. First, from the macroscopic diffusion view, $\beta=D_L/d^2$, where D_L is the liquid diffusivity and d is the atomic jump distance. To evaluate the attachment frequency for nucleation, we assume that diffusion and viscous flow follow the same physical mechanism depending on Brownian motion, and then the diffusion coefficient D_L can be obtained according to the Stokes–Einstein equation between the diffusivity and the viscosity in the below:[60]

$$D_L=\frac{kT}{3\pi a_0\eta} \tag{4}$$

where a_0 is taken as an atomic size; η is the kinematic viscosity, which can be expressed by the Vogel–Fulcher–Tamann relation:[38] $\eta=\eta_0\exp[B/(T-T_0)]$, η_0 and B are constants, and T_0 is the Kauzmann temperature. However, this indirect evaluation of β is not necessary and may not be valid when the delay time for the onset of nucleation is available through direct measurement during isothermal transformation.

Secondly, from the microscopic nucleation perspective, each of the existing clusters will grow or shrink at a rate determined by the attachment frequency across the matrix/cluster interface:

$$\beta=\frac{1}{2Z^2\tau} \tag{5}$$

where Z is Zeldovich factor; τ is the transient delay time for nucleation and is defined as the time required to establish the steady-state nucleation in a system.[61] Under the assumption that in the experimental temperature region the delay time satisfied the Arrhenius relationship, by fitting the discrete τ values, the continuous τ(T) could be obtained by

$$\tau=\tau_0\exp(\frac{Q}{RT}) \tag{6}$$

where Q is the delay time activation energy. The steady state nucleation rate J can be expressed by

$$J=\rho_s Z\beta_0\exp(-\frac{Q}{RT})\exp(-\frac{\Delta G^* f(\theta)}{kT}) \tag{7}$$

where $\beta_0=1/(2Z^2\tau_0)$. Considering that $\Delta G^*=\frac{16\pi}{3}\frac{\sigma^3}{\Delta G^2\nu}=\frac{16\pi}{3}\frac{\sigma^3 T_m{}^2}{(T_m-T)^2\Delta H^2}$, Eq. (7) can be rewritten as

$$\ln J = \ln(\rho_s \beta_0 Z) - \frac{Q}{RT} - \frac{A}{T(T_m - T)^2} \quad (8)$$

where $A = \frac{16\pi T_m^{\ 2}\sigma^3 f(\theta)}{3k\Delta H^2} = A' f(\theta)$, $A' = \frac{16\pi T_m^{\ 2}\sigma^3}{3k\Delta H^2}$. At a given temperature *T*, when one nucleation event occurs on a catalytic site of area *a* after the crystallization time *t*, the onset of crystallization can be simply defined by

$$Jat = 1 \quad (9)$$

Inserting the Eq. (9) into Eq. (8), the onset time *t* of crystallization can be expressed by

$$\ln(t) = C + \frac{Q}{RT} + \frac{A}{T(T_m - T)^2} \quad (10)$$

where $C = -\ln(\rho_s \beta_0 Z a)$. From the above experimental results, T_0=219K, T_m=627K. The melting enthalpy ΔH, can be calculated by integrating the shaded area based on the DSC heat flow curve in the insertion of the Fig. 1(b) and the value of ΔH is about $1.6*10^8 J/m^3$. Thus, based on the Eq. (10), the experimental results of A path and B path in the TTT diagram can be well fitted in the whole temperature between the glass transition temperature and the melting temperature, respectively, as is shown in the Fig. 7(a) and the detailed fitting Equations were also shown in the insertion of Fig. 7(a). Similarly, the TTT diagrams by heating from glass II and the deeply annealed glass were also well fitted by Eq. (10) and the detailed fitting can be seen in the Fig. 12(a) and 12(b).

The development of the partially overlapping TTT curves (The fitted orange and green solid curves fitted by Eq. (10)) in Fig. 7(a) provides an opportunity to evaluate the relative magnitudes of several factors in the nucleation rate expression of Eq. (7). For the evaluation, several comparison points on the TTT curves are identified as shown in Fig. 7(a). The analysis proceeds in several steps as follows. First, as described previously, by taking the glass I as an example, we provided the detailed evaluation and calculation method based on the heterogeneous nucleation model about the potential nucleation site density ρ and nucleation catalytic factor f(θ) for two potential nucleation sites. Secondly, based on the calculation results of potential nucleation site density and nucleation catalytic factor for two potential nucleation sites, we discussed the cooling rate and structural relaxation effect on the double-nosed TTT diagrams by heating from glasses by comparing the potential nucleation site density and nucleation catalytic factor for two glasses (glass I and glass II).

4.2 Evaluation of potential nucleation site density ρ for two potential nucleation sites for glass I

For Glass I, at the nose points of TTT diagram by heating from glass, point 1 and point 2 in the Fig. 7(a), the steady state nucleation rate is at a maximum so that, dln(J)/dT=0. Then, at the nose point,

$$\frac{Q}{RT^2} + \frac{A(\Delta T - 2T)}{T^2 \Delta T^3} = 0 \quad (11)$$

where $\Delta T=T_m-T$. For the path A, the value of delay time activation energy can be obtained by fitting the data of the TTT curve at the low temperature range to yield $Q_A=228\pm7$ kJ/mol; for path B, the value of delay time activation energy can be calculated by the fitted curve at the low temperature range, $Q_B=222\pm5$ kJ/mol (The detailed fitting and calculation are seen in the Fig. 6 and Fig. 11). According to the above calculations, the difference of delay time activation energy Q for these two paths is very small and within the uncertainty range, thus we assume $Q_A=Q_B$ in the following analyses. From the TTT curves in Fig. 7(a), the detailed data at point 1 and 2 are $t_1=0.076$s, $T_1=296^oC$ and $t_2=0.020$s, $T_2=255^oC$. Therefore, according to the Eq. (11) and the above experimental results, information can be obtained about the interfacial energy between liquid and solid and the contact angle between the nucleus and the catalytic substrate: $\sigma_1^3 f(\theta_1)=9.675*10^{-7}$ J^3/m^6 and $\sigma_2^3 f(\theta_2)=2.892*10^{-6}$ J^3/m^6. Considering the same crystalline products for path A and path B in Fig. 5(c), the values of σ_1 and σ_2 should be same. Thus, the ratio of $f(\theta_1)$ for path A and $f(\theta_2)$ for path B can be calculated, about 0.335. It should be noted that, when we consider $f(\theta_1)=0.1$, which would represent a low potency site as expected for bulk glass formation, the estimated value for σ is 21.3 mJ/m^2. The value of the interfacial energy σ for Zn-based MG is comparable with values for other MG systems with similar crystalline phases containing icosahedral arrangements, for example, $\sigma=40$ mJ/m^2 for $Zr_{41.2}Ti_{13.8}Cu_{12.5}Ni_{10}Be_{22.5}$ ($T_L=1026$K), 67 mJ/m^2 for $Pd_{40}Ni_{10}Cu_{30}P_{20}$ ($T_L=823$K) and 14 J/m^2 for $Zr_{60}Co_{30}Al_{10}$ ($T_L=925$K).[38, 60-62] In these MG systems, the relatively low σ value implies a low nucleation barrier and a high nucleation rate (For Zn-based MG in this work, the onset crystallization microstructure of Flash DSC sample at 330°C by TEM is illustrated in the Fig. 5(d) and it displays a complex pattern of the few product phases with a high density consistent with a high nucleation rate). Thus, in these cases, glass formation is linked to the delay time.

For further analysis, we consider the nose points 1 and 2 and for the onset of crystallization according to Eq. (9), $J_1at_1=J_2at_2=1$. Thus, for sites with comparable a,

$$\frac{J_1}{J_2}=\frac{t_2}{t_1} \tag{12}$$

Then according to Eq. (7), Eq. (12) can be expressed as

$$\frac{t_2}{t_1}=\frac{\rho_A}{\rho_B}\exp(-\frac{\Delta G_1^* f(\theta_1)}{kT_1}+\frac{\Delta G_2^* f(\theta_2)}{kT_2}) \tag{13}$$

Therefore, the ratio value of the density of the potential nucleation sites for the A and B kinetic paths can be obtained as

$$\frac{\rho_A}{\rho_B}=\frac{t_2}{t_1}\exp\{\frac{16\pi T_L^{\ 2}}{3k\Delta H^2}[\frac{\sigma_1^{\ 3} f(\theta_1)}{T_1(T_m-T_1)^2}-\frac{\sigma_2^{\ 3} f(\theta_2)}{T_2(T_m-T_2)^2}]\} \tag{14}$$

Based on the above expression, after substitution of the evaluated parameters, the site density ratio is obtained as $\rho_{A\text{-}10000}/\rho_{B\text{-}10000}\approx0.028$ and the density of potential path B nucleation site is much larger than that for the path A nucleation site for glass I.

4.3 Evaluation of nucleation catalytic factor f(θ) for two nucleation sites for glass I

At the same annealing temperature, for the point A in path A and the point B in path B in Fig. 7(a), $J_A at_A = J_B at_B$ and then $J_A t_A = J_B t_B$. According to Eq. (7), and considering that $Q_A = Q_B$ and $T_A = T_B$, then

$$\rho_A \exp(-\frac{\Delta G^*_A f(\theta)_A}{kT}) t_A = \rho_B \exp(-\frac{\Delta G^*_B f(\theta)_B}{kT}) t_B \quad (15)$$

Eq. (15) can be rewritten as

$$\Delta G^*_B f(\theta)_B - \Delta G^*_A f(\theta)_A = kT[\ln(\frac{\rho_B}{\rho_A}) + \ln t_B - \ln t_A] \quad (16)$$

After substitution by the detailed fitting curves of $\ln(t_A)$ and $\ln(t_B)$ in Fig. 7(a), Eq. (16) can be plotted in Fig. 7(b). By comparing the TTT diagram in Fig. 7(a) and Fig. 7(b), there exist two different potential nucleation sites, site A and site B for the Zn-based MG. In both the low temperature and high temperature range, $\Delta G^* f(\theta)$ for site A is lower than that of site B and the site A controls the nucleation path; at intermediate temperature, $\Delta G^* f(\theta)$ for site B is lower than that of site A and the site B controls the nucleation path. Especially, at the intersection between site A and site B of TTT curves, the points 3 and 4 in Fig. 7(a), the relation $\Delta G^*_B f(\theta)_B = \Delta G^*_A f(\theta)_A$ holds and so that $[f(\theta)_B = f(\theta)_A]_3$, $[f(\theta)_B = f(\theta)_A]_4$, which are self-consistent results.

For nucleation site A and site B, to compare the difference of $f(\theta)$ at the low and high temperature range with the same onset crystallization time, the value of $\ln(t) = -2.167$ ($t = 0.1145$s) was selected and the temperatures at the low and the high range for path A and path B are set by points 5, 6 and points 7, 8 in Fig. 7(a). For path A, at the same delay time t, points 5 and 6 have the same t, Q, σ and A'. Thus, $J_5 = J_6$, and then from the Eq. (7),

$$\frac{f(\theta)_5}{T_5 \Delta T_5^2} - \frac{f(\theta)_6}{T_6 \Delta T_6^2} = \frac{Q_A}{A' R}(\frac{1}{T_6} - \frac{1}{T_5}) \quad (17)$$

Similarly, for path B,

$$\frac{f(\theta)_7}{T_7 \Delta T_7^2} - \frac{f(\theta)_8}{T_8 \Delta T_8^2} = \frac{Q_B}{A' R}(\frac{1}{T_8} - \frac{1}{T_7}) \quad (18)$$

From the experimental TTT curve and the fitted curves in Fig. 7(a), the detailed data of (ln(t), T) for points 5, 6, 7 and 8 can be obtained, and the Eqs. (17) and (18) can be evaluated as

$$\frac{f(\theta)_5}{2.44} - \frac{f(\theta)_6}{10.53} = 3.23 \times 10^{-7} \frac{1}{\sigma^3} \quad (19)$$

$$\frac{f(\theta)_7}{5.95} - \frac{f(\theta)_8}{13.63} = 2.88 \times 10^{-7} \frac{1}{\sigma^3} \quad (20)$$

For amorphous alloys, the values of $f(\theta)$ and σ usually exhibit some dependence on temperature[38-39] so that there should exist some difference between $f(\theta)_5$ and $f(\theta)_6$, and $f(\theta)_7$ and

$f(\theta)_8$. Interestingly, when the difference of $f(\theta)_5$, $f(\theta)_6$ and $f(\theta)_7$, $f(\theta)_8$ is assumed to be negligible, so that $f(\theta)_5=f(\theta)_6= f(\theta)_A$ and $f(\theta)_7=f(\theta)_8= f(\theta)_B$. Then, the Eqs. (19) and (20) can be expressed as

$$\sigma^3 f(\theta)_A(\frac{1}{2.44}-\frac{1}{10.53}) = 3.23\times10^{-7} \quad (21)$$

$$\sigma^3 f(\theta)_B(\frac{1}{5.95}-\frac{1}{13.63}) = 2.88\times10^{-7} \quad (22)$$

When the previous calculated values of $f(\theta)_1\sigma_1^3$ and $f(\theta)_2\sigma_2^3$ are substituted into the left sides of Eq. (21) and Eq. (22), the values of left sides of Eq. (21) and (22) are 3.04×10^{-7} and 2.73×10^{-7}, which yields a close match with the values of right sides. The small difference of both sides for Eq. (21) and Eq. (22) indicates the small temperature dependence of σ and f(θ). Furthermore, when the values of f (θ) for points 5 and 7 and points 6 and 8 are compared, the results indicate the values of f(θ) for points 5 and 7 and points 6 and 8 are significantly different. Therefore, from the above analysis, for the same nucleation site, the values of f(θ) at high and low temperatures are close in value for one onset crystallization time; for two different nucleation paths A and B with different potential site densities, the values of f(θ) at high and low temperatures are different.

4.4 Cooling rate and structural relaxation effects on the potential nucleation site density ρ and nucleation catalytic factor f(θ) for two nucleation sites

Following the previous calculation methods, for glass II, the site density ratio between site A and site B is obtained as $\rho_{A\text{-}3000}/\rho_{B\text{-}3000}\approx0.163$. One can clearly see that the density of potential nucleation site B is also larger than that for the nucleation site A for glass II, which is similar with that of glass I. By comparing the ratio values between two glasses, the only difference is that the potential site density ratio of two nucleation sites for glass I is larger than that of glass II, which indicates that the site density difference for two nucleation sites decreases with the decrease of the cooling rate. To further investigate the evolution of site density for two nucleation sites with cooling rate, the ratios of site density for site A and site B were separately calculated . The values of the site density ratio of site A and site B for glass I and glass II $\rho_{A\text{-}10000}/\rho_{A\text{-}3000}$ and $\rho_{B\text{-}10000}/\rho_{B\text{-}3000}$ are 0.317 and 1.852. From these two values, compared to the glass I with larger cooling rate, the nucleation site density of site A for glass II with smaller cooling rate increases and the nucleation site density of site B for glass II decreases. Based on the above calculation results about the site density ratio of site A and site B for glass I and glass II, $\rho_{A\text{-}10000}/\rho_{A\text{-}3000}$, $\rho_{B\text{-}10000}/\rho_{B\text{-}3000}$, $\rho_{A\text{-}10000}/\rho_{B\text{-}10000}$ and $\rho_{A\text{-}3000}/\rho_{B\text{-}3000}$, we can get the value of the total site density ratio for glass I and glass II $\rho_{\text{-}3000}/\rho_{\text{-}10000}=(\rho_{A\text{-}3000}+\rho_{B\text{-}3000})/(\rho_{A\text{-}10000}+\rho_{B\text{-}10000})\approx1.52$. It is surprising to find that the calculation value of $\rho_{\text{-}3000}/\rho_{\text{-}10000}$ by heating from glasses with cooling rates of 3000 K/s and 10000 K/s is very close to the value of the total nucleation site density ratio by cooling from liquid with cooling rates of 3000 K/s and 10000 K/s, 1.63, which further verifies that the potential nucleation sites during heating from glass originated from the quenched-in clusters during the cooling down process. Moreover, as shown by the red arrows in Fig. 6, the nose point temperature for site A for glass II barely change compared to the nose point for site A for glass I; in contrast, the nose point temperature for site B for glass II shifts to the higher temperature compared to the nose point for site B for glass I, which means the two nucleation paths gradually draw closer with the decrease of cooling rate. For the annealed glass sample, we can also calculate the ratio between the site density for deeply annealed glass and the site density of site A for glass I, $\rho_{GlassI\text{-}A}/\rho_{Annealed}\approx0.097$,

and then the ratio between the site densities for site A of glass I and glass II and the site density for annealed glass is $\rho_{GlassI\text{-}A} : \rho_{GlassI\text{-}A} : \rho_{Annealed}$ =1:3.15:10.34. From this ratio, the site density for the annealed glass sample is much larger than that of the as-cast samples, which is consistent with the previous results from the quenched-in nuclei model.

For glass II as for the glass I, the values of f(θ) at high and low temperatures for the same nucleation site are close in value for one onset crystallization time; for two different nucleation paths A and B with different potential site densities, the values of f(θ) at high and low temperatures are different. For the annealed glass, the values of f(θ) at high and low temperatures are close in value for one onset crystallization time. Moreover, to investigate the cooling rate and the structural relaxation effects on the nucleation catalytic factor f(θ) for two potential nucleation sites, we examined the interfacial energy σ and the catalytic factor f(θ) of each nucleation site for three glass samples. For each nucleation site for one glass, considering that the weak temperature dependence of $\sigma^3 f(\theta)$, the values of $\sigma_1{}^3 f(\theta_1)$, $\sigma_{1'}{}^3 f(\theta_{1'})$, $\sigma_2{}^3 f(\theta_2)$, $\sigma_{2'}{}^3 f(\theta_{2'})$ and $\sigma_{1''}{}^3 f(\theta_{1''})$ can be used to estimate the correlation of σ and f(θ). Then, the plots of σ and f(θ) of nucleation sites A and B for glass I, glass II and the annealed glass are exhibited in the Fig. 8. To quantitatively compare the value change of f(θ) for three glasses, we selected one σ of 21.3 mJ/m^2 as marked by the dark-yellow line in Fig. 8. For glass I, the value of f(θ) for site A is larger than that of site B, which indicates that the heterogeneous nucleation events for site B is less catalytic than those for site A, which is consistent with the TEM results in Fig. 5(d). The similar results exist in glass II. However, both values of f(θ) for site A and site B in glass II are smaller than those of glass I, which indicates that the nucleation events in glass II become more catalytic. Moreover, the change of f(θ) for site B is much larger than that of site A, which implies that the cooling rate effect is more evident for site B than site A. It should be noted that the difference of f(θ) for site A and site B in glass I is larger than that in glass II. For the annealed glass sample, the value of f(θ) continues to decrease compared to those of the site A for glass I and glass II, which indicates that the annealed glass sample tends to the more catalytic nucleation.

5. Conclusions

In conclusion, the thermal stability and nucleation kinetics have been characterized for a strong Zn-based MG system based on the Flash DSC with ultrafast heating and cooling rate. A unique double-nose-shaped TTT diagram is found by a series of isothermal tests by fast heating into the target temperature from glass state, which implies that there exists a novel crystallization pathway in MGs. This novel transformation path is verified to be induced by two different heterogeneous nucleation sites that can originate from the intrinsic structural heterogeneity of MGs. The decrease of the cooling rate and the structural relaxation induce the TTT diagram to shift to the shorter time range, which indicates that the nucleation and crystallization behaviors can be tuned by designing the structural heterogeneities in MGs. Moreover, the kinetics measurements provide a basis for a heterogeneous nucleation model that accounts for the observed multiple crystallization processes and the cooling rate and structural relaxation effect on the nucleation kinetic behavior evolution in amorphous materials. With the application of the Flash DSC method, it seems likely that novel crystallization behaviors can be discovered in other MG systems.

References

[1] W. L. Johnson, MRS Bull. **24**, 42 (1999).

[2] M. W. Chen, NPG Asia Mater. **3**, 82 (2011).

[3] C. Suryanarayana, A. Inoue, Bulk metallic glasses. CRC PRESS. New York, 2011.

[4] C. A. Schuh, T. C. Hufnagel, U. Ramamurty, Acta Mater. **55**, 4067 (2007).

[5] B. Zhang, D. Q. Zhao, M. X. Pan, W. H. Wang, A. L. Greer. Phys. Rev. Lett. **94**, 205502 (2005).

[6] G. Kumar, H.X. Tang, J. Schroers, Nature, **457**, 868 (2009) .

[7] G. Kumar, A. Desai, J. Schroers, Adv. Mater. **23**, 461 (2011) .

[8] Y. C. Chen, J. P. Chu, J. S. C. Jang, C. W. Wu, Mater. Sci. Eng. A, **56**, 488 (2012) .

[9] J. F. Li, D. Q. Zhao, M. L. Zhang, W.H. Wang, Appl. Phys. Lett. **93**, **171907** (2008).

[10] K. Zhao, J. F. Li, D. Q. Zhao, M. X. Pan, W. H. Wang, Appl. Phys. Lett. **98**, 141913 (2011).

[11] S. Pogatscher, P. J. Uggowitzer, J. F. Loffler, Appl. Phys. Lett. **104**, 251908 (2014).

[12] W. Jiao, K. Zhao, X. K. Xi, D.Q. Zhao, M. X. Pan, W. H. Wang, J. Non-cryst. Solids, **356**, 1867 (2010).

[13] D. C. Hofmann, Jin-Yoo. Suh, A. Wiest, G. Duan, M. L. Lind, M. D. Demetriou, W. L. Johnson, Nature **451**, 1085 (2008).

[14] Y. Wu, Y. Xiao, G. Chen, C. T. Liu, Z. Liu, Adv. Mater. **22**, 2770 (2010).

[15] A. L. Greer, Mater. Sci. Eng. A, **304**, 68 (2001).

[16] J. C. Ye, J. Lu, C. T. Liu, Q. Wang, Y. Yang, Nat. Mater. **9**, 619 (2010).

[17] H. Wagner, D. Bedorf, S. Kuchemann, M. Schwabe, B. Zhang, W. Arnold, K. Samwer, Nat. Mater. **10**, 439 (2011).

[18] Z. Wang, P. Wen, L. S. Huo, H. Y. Bai, W. H. Wang, Appl. Phys. Lett. **101**, 121906 (2012).

[19] L. S. Huo, J. F. Zeng, W. H. Wang, C. T. Liu, Y. Yang, Acta Mater. **61**, 4329 (2013).

[20] T. Ichitsubo, E. Matsubara, Yamamoto, H. S. Chen, N. Nishiyama, J. Saida, K. Anazawa, Phys. Rev. Lett. **95**, 245501 (2005).

[21] S. T. Liu, Z. Wang, H. L. Peng, H. B. Yu, W. H. Wang, Scr. Mater. **67**, 9 (2012).

[22] E. Zhuravlev, C. Schick, Thermochim. Acta **505**, 1 (2010).

[23] E. Zhuravlev, C. Schick, Thermochim. Acta **505**, 14 (2010).

[24] V. Mathot, M. Pyda, T. Pijpers, G. Vanden Poel, E. Van De Kerkhof, S. Van Herwaarden, F. Van Herwaarden, A. Leenaers, Thermochim. Acta **522**, 36 (2011).

[25] P. Cebe, B. P. Partlow, D.L. Kaplan, A. Wurm, E. Zhuravlev, C. Schick, Thermochim. Acta **615**, 8 (2015).

[26] J. Orava, A.L. Greer, B. Gholipour, D.W. Hewak, C.E. Smith, Nat. Mater. **11**, 279 (2012).

[27] E. Parodi, L. E. Govaert, G. W. M. Peters, Thermochim. Acta **657**, 110 (2017).

[28] S. Pogatscher, D. Leutenegger, A. Hagmann, P. J. Uggowitzer, J. F. Löffler, Thermochim. Acta **509**, 84 (2014).

[29] S. Pogatscher, D. Leutenegger, A. Hagmann, P. J. Uggowitzer, J. F. Löffler, Nat. Comm. **7**, 11113 (2016).

[30] J. Q. Wang, Y. Shen, J. H. Perepezko, M. D. Ediger, Acta Mater. **104**, 25 (2016).

[31] F. X. Bai, J. H. Yao, Y. X. Wang, J. Pan, Y. Li, Scr. Mater. **132**, 58 (2017).

[32] S. Pogatscher, D. Leutenegger, J. E. K. Schawe, P. Maris, R. Schaublin, P. J. Uggowitzer, J. F. Löffler, J. Phys.: Condens. Matter. **30**, 234002 (2018).

[33] C. A. Angell, Science **267**, 1924 (1995).

[34] M. D. Ediger, C. A. Angell, Sidney R. Nagel, J. Phys. Chem. **100**, 13200 (1996).

[35] B. Zhang, R. J. Wang, D. Q. Zhao, M. X. Pan, W. H. Wang, Phys. Rev. B, **70**, 224208 (2004).

[36] B. A. Legg, J. Schroers, R. Busch , Acta Mater. **55**, 1109 (2007).

[37] J. C. Qiao, J. M. Pelletier, Q. Wang, W. Jiao, W.H. Wang, Intermetallics **19**, 1367 (2011); J. C. Qiao, R. Casalini, J. M. Pelletier, Y. Yao, J. Non-cryst. Solids **447**, 85 (2016).

[38] J. F. Loffler, J. Schroers, W. L. Johnson, Appl. Phys. Lett. **77**, 681 (2000).

[39] C. C. Hays, J. Schroers, W. L. Johnson, T. J. Rathz, R. W. Hyers, J. R. Rogers, M. B. Robinson, Appl. Phys. Lett. **79**, 1605 (2001).

[40] D. H. Xu, W. L. Johnson, Phys. Rev. B **74**, 024207 (2006).

[41] A. Masuhr, T. A. Waniuk, R. Busch, W. L. Johnson, Phys. Rev. Lett. **82**, 2290 (1999).

[42] J. E. K. Schawe, P. A. Vermeulen, M. V. Drongelen, Thermochim. Acta **616,** 87 (2015).

[43] A. M. Rhoades, N. Wonderling, C. Schrick, R. Androsch, Polymer, **106**, 29 (2016).

[44] G. Wilde, H. Sieber, J. H. Perepezko, Scr. Mater. **40**, 779 (1999).

[45] J. H. Perepezko, Prog. Mater. Sci. **49**, 263 (2004).

[46] W. G. Stratton, J. Hamann, J. H. Perepezko, P. M. Voyles, X. Mao, S. V. Krare, Appl. Phys. Lett. **86**, 141910 (2005).

[47] J. Ding, Y. Q. Cheng, E. Ma, Acta Mater. **69**, 343 (2014).

[48] L. Yang, G. Q. Guo, L. Y. Chen, B. LaQua, J. Z. Jiang, Intermetallics **44**, 94 (2014).

[49] R. E. Ryltsev, B. A. Klumov, N. M. Chtchelkatchev, K. Y. Shunyaev, J. Chem. Phys. **145**, 034506 (2016).

[50] J. H. Perepezko, K. Hildal, Philos. Mag. **86**, 3681 (2006).

[51] J. H. Perepezko, C. Santhaweesuk, J. Q. Wang, S. D. Imhoff, J. Alloys Compd. **615**, 192 (2014).

[52] F. Zhu, S. X.Song, K. M. Reddy, A. Hirata, M.W. Chen, Nat. Comm. **9**, 3965 (2018).

[53] Y. Yang, J. F. Zeng, A. Volland, J. J. Blandin, S. Gravier, C. T. Liu, Acta Mater. **60**, 5260 (2012).

[54] P. G. Debenedetti, F. H. Stillinger, Nature **410**, 259 (2001).

[55] Z. Evenson, T. Koschine, S. Wei, O. Gross, J. Bednarcik, I. Gallino, J. J. Kruzic, K. Ra¨tzke, F. Faupel, R. Busch, Scr. Mater. **103**, 14 (2015).

[56] Z. W. Wu, M. Z. Li, W. H. Wang, K. X. Liu, Phys. Rev. B **88**, 054202 (2013).

[57] L. Battezzati, Mater. Sci. Eng. A **60**, 375 (2004).

[58] H. J. Fecht, J. H. Perepezko, M. C. Lee, W. L. Johnson, J. Appl. Phys. **68**, 4494 (1990).

[59] W. J. Boettinger, J. H. Perepezko, in: H. H. Liebermann (Ed.), Rapidly Solidified Alloys: Processes, Structures, Properties, Applications, vol. 17, Marcel Dekker Inc., Parsippany, NJ, 1993.

[60] M. C. Weinberg, D. R. Uhlmann, E. D. Zanotto, J. Am. Ceram. Soc. **72**, 2054 (1989).

[61] Y. T. Zhu, T.C. Lowe, R.J. Asaro, J. Appl. Phys. **82**, 1129 (1997).

[62] Z. Wang, S. V. Ketov, C. L. Chen, Y. Shen, Y. Ikuhara, A. A.Tsarkov, D. V. Louzguine-Luzgin, J. H. Perepezko, Acta Mater. **132**, 298 (2017).

Table 1. Thermodynamic properties of Zn-based metallic glass ribbon measured by normal DSC (20K/min, the detailed heat flow curve is given in the Fig. 1(b): glass transition temperature T_g, crystallization temperature T_{x1}, T_{x2} and T_{x3}, the melting temperature T_m and the liquidus temperature T_L, the kinetic fragility *m*, the critical cooling rate range R_c and the critical heating rate R_h.

T_g (K)	T_{x1} (K)	T_{x2} (K)	T_{x3} (K)	T_m (K)	T_L (K)	*m*	R_c (K/s)	R_h (K/s)
393	432	450	522	627	666	46	1900-2000	15000

Table 2. Crystallization enthalpies corresponding to different heating rates for one same Flash DSC sample. The value of crystallization enthalpy is calculated by integrating the area of the crystalline peak in Fig. 2(c).

Cooling rate (K/s)	Enthalpy (μJ)
750	0.166
775	0.51
800	0.90
815	1.15
1025	9.89
1075	13.40
1250	25.03
1400	34.26
1410	35.42
1425	36.95
1475	38.72
1510	40.79
1775	50.22
1810	50.88
1845	51.38
1900	53.50
1950	54.46
2000	54.88
2100	58.06
2150	57.04
2200	58.23
2250	58.58
2350	58.22
2500	58.34
2750	58.93
3000	59
3250	58.7
3500	58.53
3750	58.29

Table 3. The values of the fitting parameters for TTT diagrams by cooling from liquid with different cooling rates based on Eq. (S4). The detailed fitting expressions are inserted in the Fig. 6(b).

R_c (K/s)	Γ	B	C
3000	-4.08	1498.72	1.14×10^7
10000	-3.59	1475.75	1.47×10^7

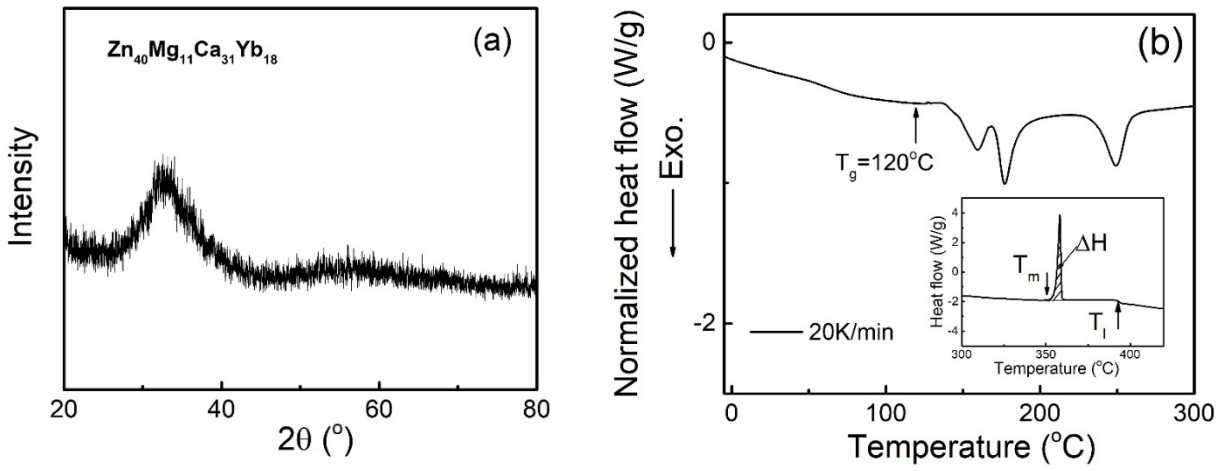

FIG. 1. (a) XRD curve displays the broad peak of Zn-based metallic glass, indicating that the sample is amorphous. (b) Typical DSC heat flow curve at the heating rate of 20K/min.

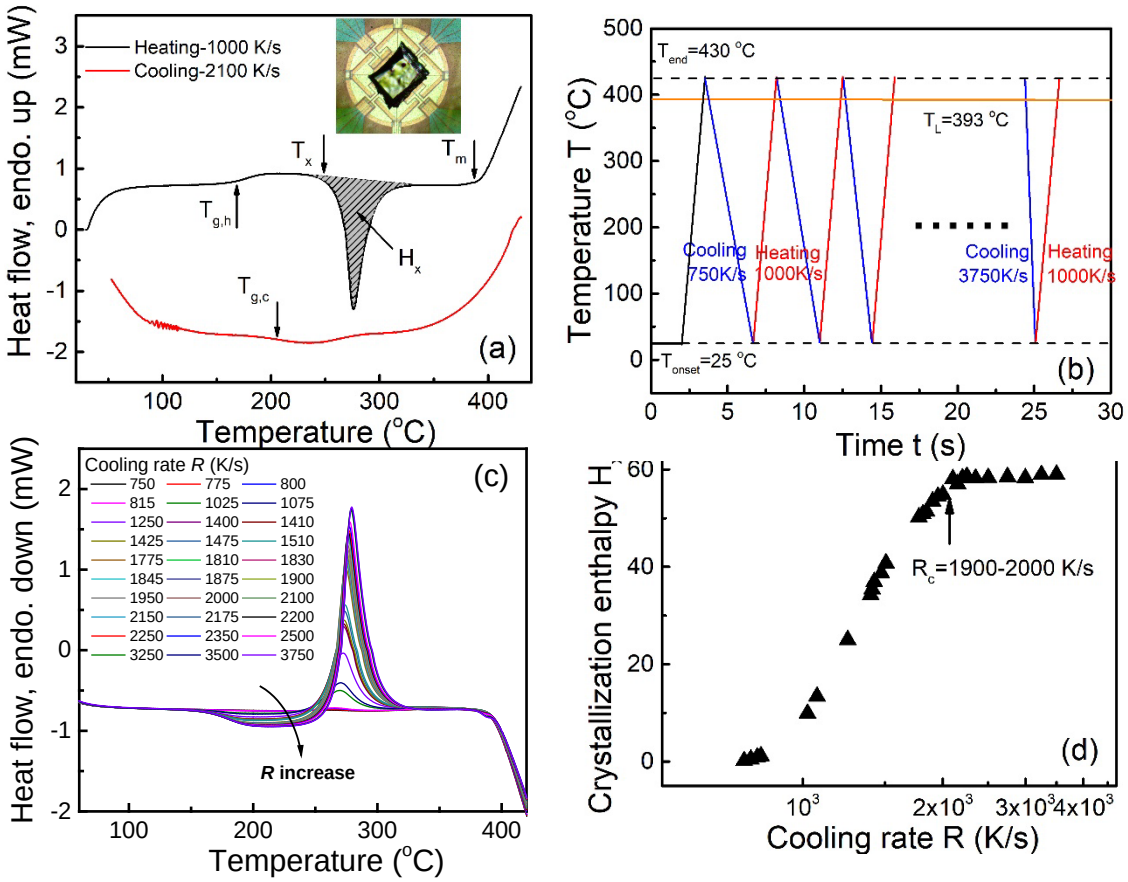

FIG. 2. (a) A representative Flash DSC trace upon heating (black) and cooling (red). (b) Schematic illustration for the applied temperature-time program to confirm the critical cooling rate range. (c) Heat flow curves corresponding to different cooling rates with a common heating rate of 1000K/s. (d) The H_x of one single sample cooled at various rates.

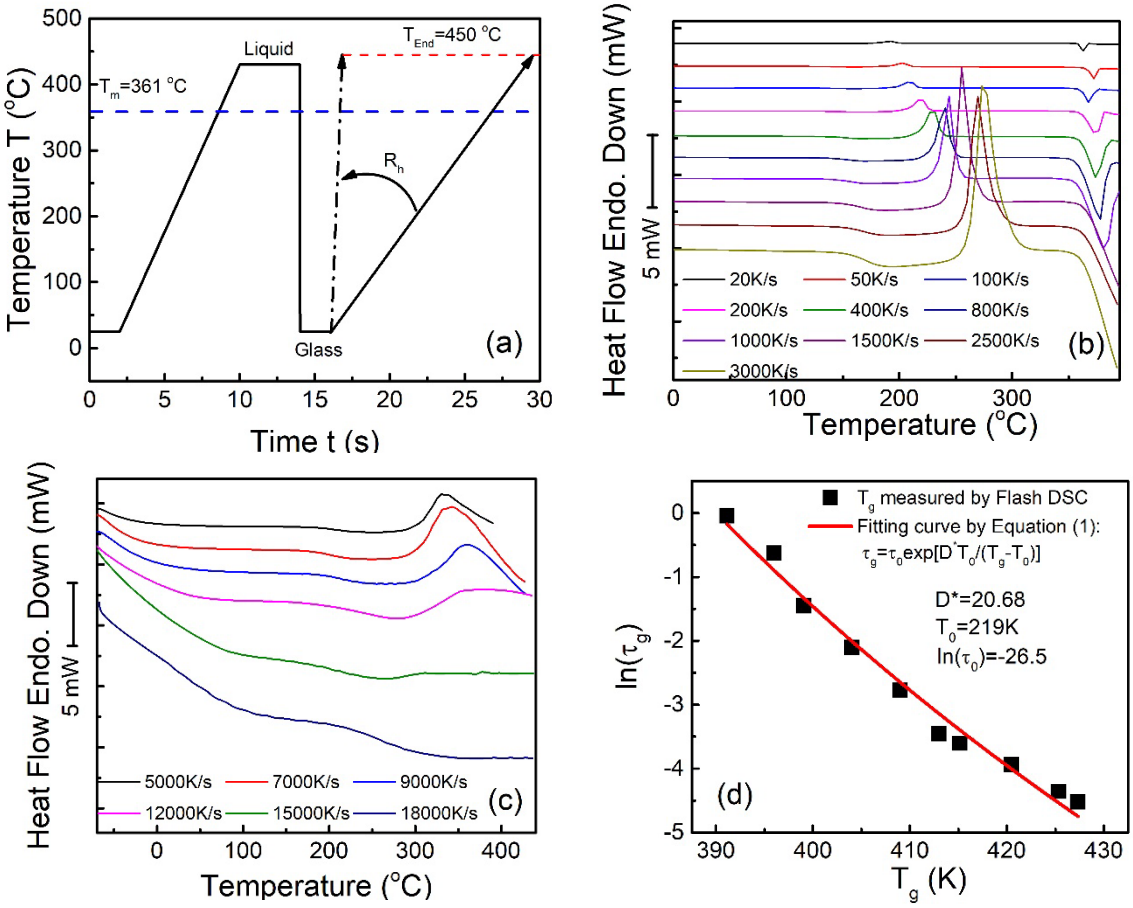

FIG. 3. (a) Schematic illustration for the applied temperature-time program to confirm the critical heating rate. (b) Heating the Zn-based metallic glass to the equilibrium liquid with rates of 20 K/s to 3000 K/s. (c) Heating the Zn-based metallic glass to the equilibrium liquid with rates of 5000 K/s to 18000 K/s. (d) The T_g and the corresponding R plot. The red curve is the fitting curve by VFT Eq. (1) and the fitting parameters are shown in the insertion of Fig. 3(d).

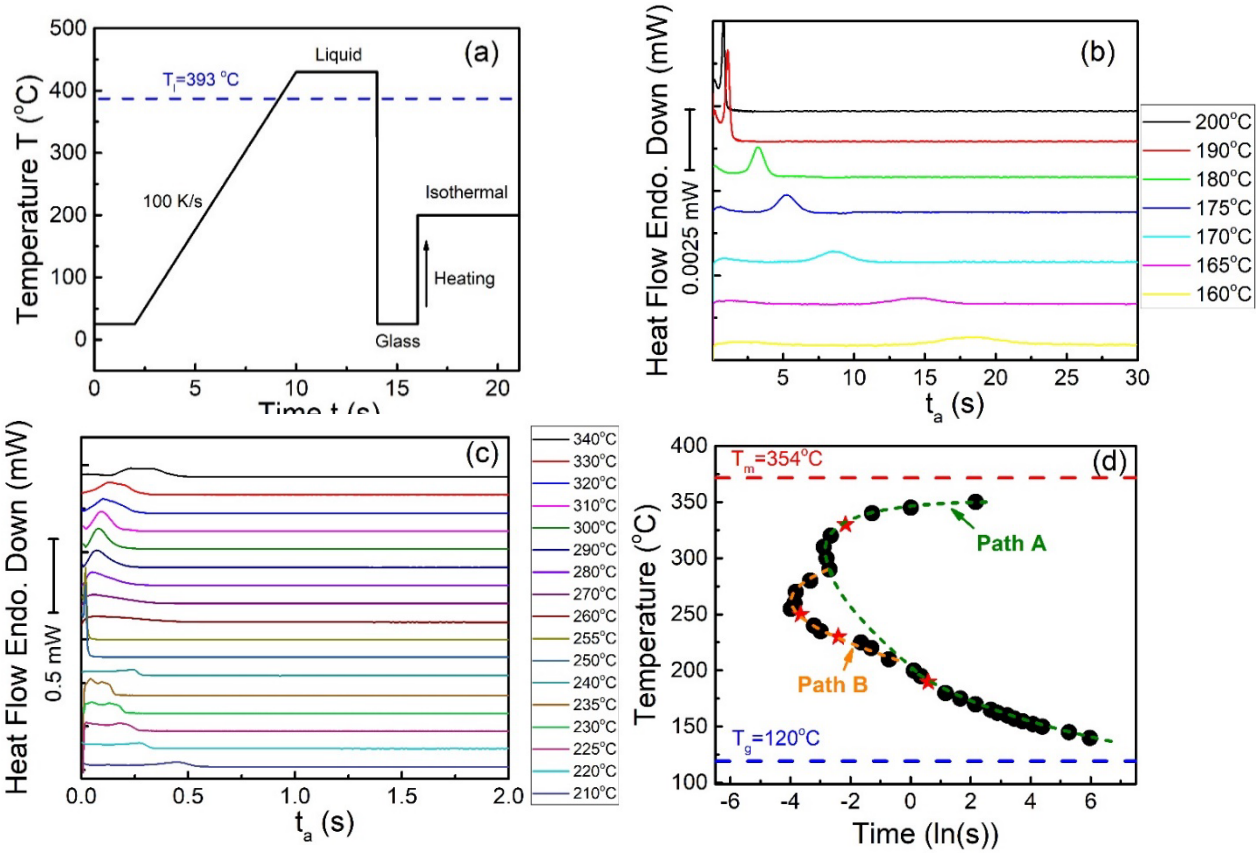

FIG. 4. (a) The applied temperature-time programs for isothermal experiments. (b) Isothermal heat flow curves at the low annealing temperature range from 160°C to 200°C according to method (1). (c) Isothermal heat flow curves at the high annealing temperature range from 210°C to 340°C according to method (1). (d) TTT diagram for Zn-based MG based on the measured data shown in Fig. 4(b) and 4(c). The orange and green dashed curves are the indicative curves following different transformation paths at different temperature ranges. The red star points give the selected four points with different temperature ranges.

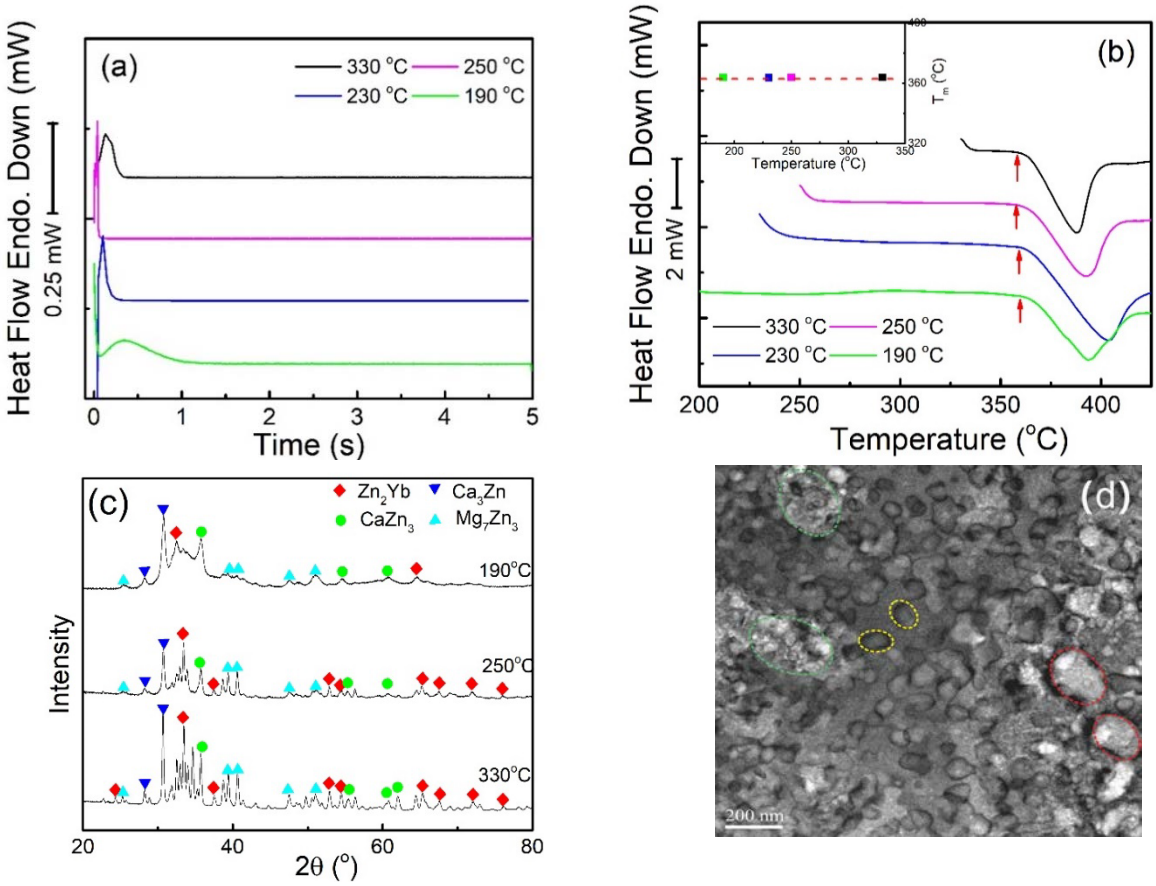

FIG. 5. (a) Isothermal heat flow curves at four different annealing temperatures: 190ºC, 230ºC, 250ºC and 330ºC. (b) Heat flow cures with heating rate of 1000K/s for four different annealed samples in Fig. 5(a). The inserted graph gives the measured T_m and the isothermal temperature T_a and the red dashed line indicates the T_m for four annealing temperature are almost the same. (c) XRD comparison for Flash DSC samples annealed at 190ºC, 250ºC and 330ºC. (d) Microstructure of onset crystalline Flash DSC sample at 330ºC by TEM.

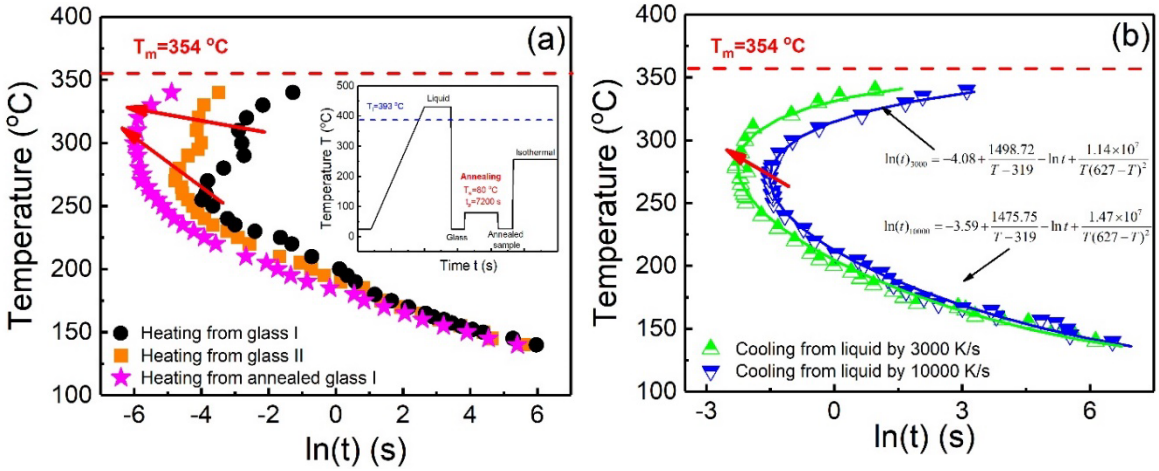

FIG. 6. (a) TTT diagram comparison for Zn-based MG by heating from glass I, glass II and the annealed glass sample. (b) TTT diagram comparison for Zn-based MG by cooling from liquid with cooling rates of 3000 K/s and 10000 K/s. The red arrows give the evolution direction of the nose points. The blue and green curves in Fig. 6(b) are the fitted curves by Eq. (S4).

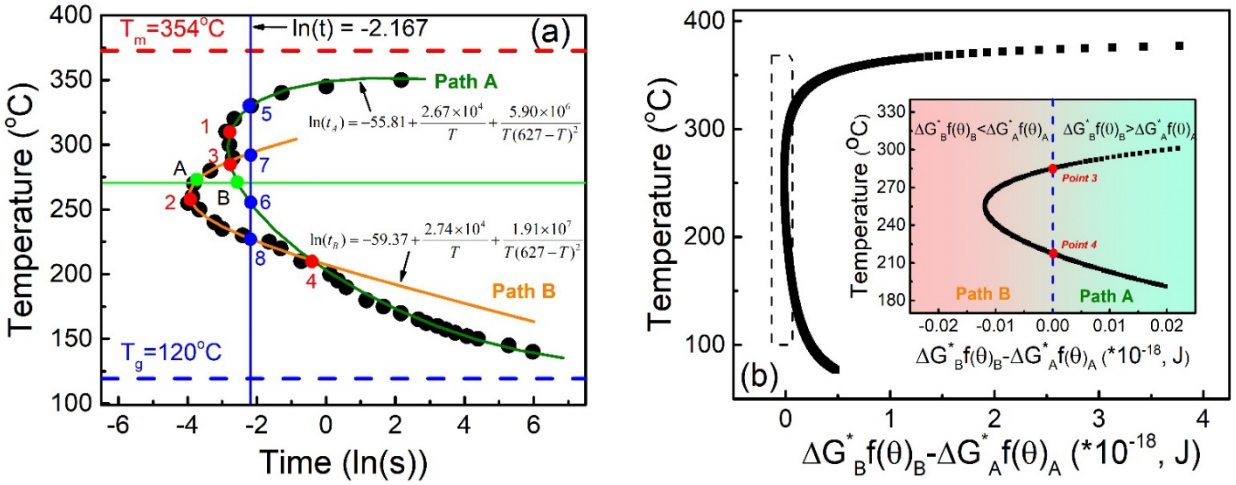

FIG. 7. (a) TTT diagram. The orange and green solid lines are the fitting curves by Eq. (10) at different temperature ranges, the two green points (A and B) are the intersection points between the fitted TTT curves and the isothermal line (green line), point 1 and point 2 are nose points for two paths and point 3 and point 4 are the intersection points between these two fitted curves. The four blue points (5, 6, 7 and 8) are the intersection points between the fitted TTT curves and the line of ln(t) = -2.167 (blue line). (b) The plot is based on the Eq. (16). The inserted graph gives the detailed part marked by a dashed rectangle.

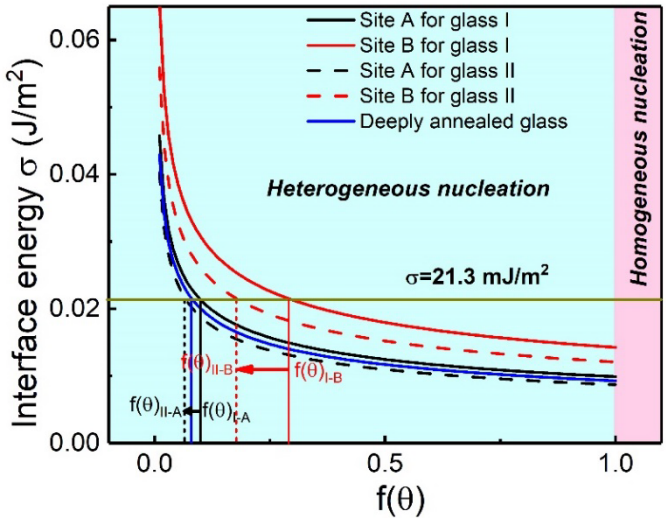

FIG. 8. Correlation of the interfacial energy σ and the catalytic factor f(θ) for site A and site B in glass I, glass II and the annealed glass.

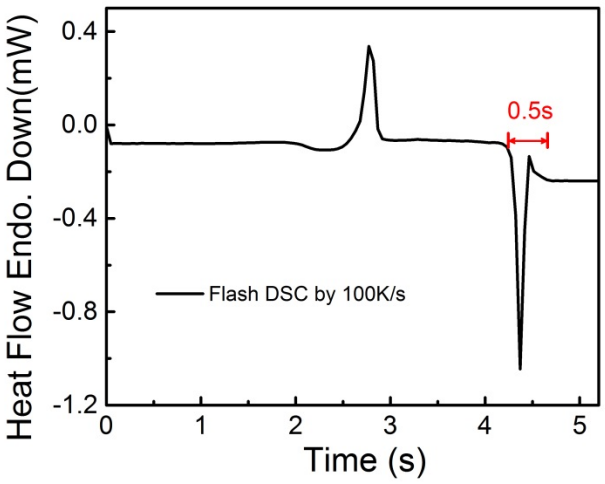

FIG. 9. Heat flow and heating time by Flash DSC at the heating rate of 100 K/s. The time of the whole melting process is about 0.5 s.

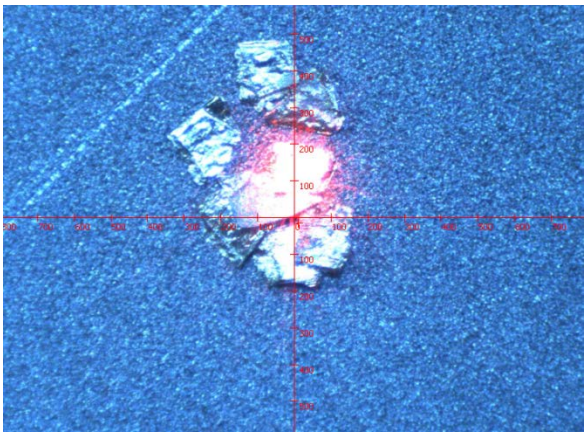

FIG. 10. Optical picture of Flash DSC samples in XRD instrument. The red spot is the laser fixing point to focus.

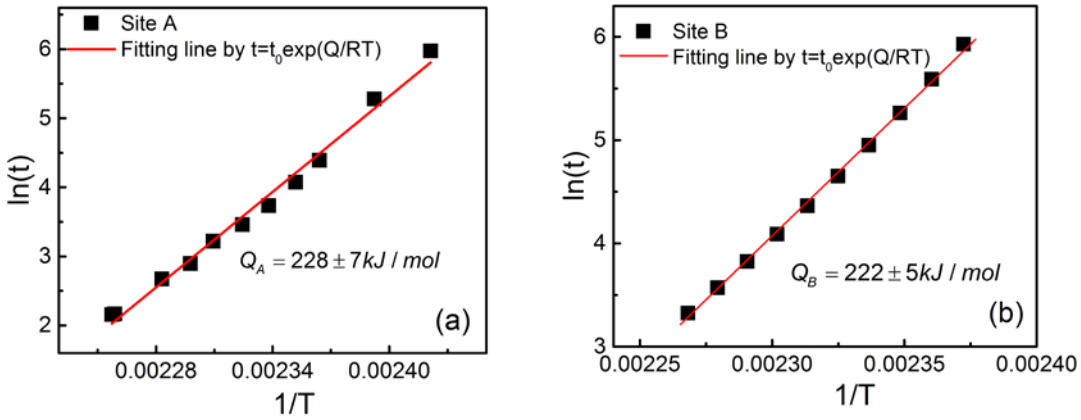

FIG. 11. (a) Delay time ln(t) for site A as a function of the annealing temperature 1/T at the low temperature range. The delay time activation energy Q can be obtained by fitting the equation of $t=t_0\exp(Q/RT)$, Q_A=228±7 kJ/mol. (b) Delay time ln(t) for site B as a function of the annealing temperature 1/T and the values of data are from the fitted TTT curve in Figure 5a. The delay time activation energy Q can be obtained by fitting the equation of $t=t_0\exp(Q/RT)$, Q_B=222±5 kJ/mol.

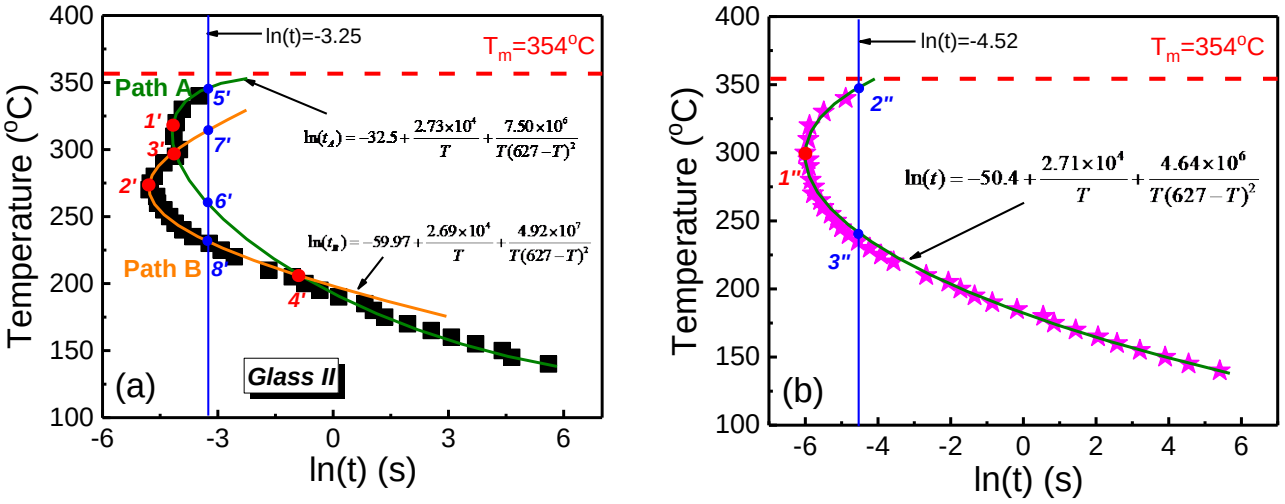

FIG. 12. (a) TTT diagram by heating from glass II. The green and orange curves are the fitted curves by Eq. (10). (b) TTT diagram by heating from the annealed glass sample. The blue curve is the fitted curve by Eq. (10).